IMK/IAA MIPAS retrievals version 8: CH_4 and N_2O

Norbert Glatthor[1], Thomas von Clarmann†[1], Bernd Funke[2], Maya García-Comas[2], Udo Grabowski[1], Michael Höpfner[1], Sylvia Kellmann[1], Michael Kiefer[1], Alexandra Laeng[1], Andrea Linden[1], Manuel López-Puertas[2], and Gabriele P. Stiller[1]

[1]Karlsruhe Institute of Technology, Institute of Meteorology and Climate Research, Karlsruhe, Germany
[2]Instituto de Astrofísica de Andalucía, CSIC, Granada, Spain

Correspondence: Norbert Glatthor (norbert.glatthor@kit.edu)

Abstract. Using the IMK/IAA data processor, methane and nitrous oxide distributions were retrieved from version 8 limb emission spectra recorded with the Michelson Inferferometer for Passive Atmospheric Sounding (MIPAS). The data set includes measurements from the Nominal, UTLS-1, Middle Atmosphere, Upper Atmosphere and Noctilucent Cloud observation modes. The processing differs from the previous version 5 data with respect to the atmospheric state variables that are jointly retrieved along with the target gases CH_4 and N_2O, the treatment of the radiance offset, the selection of microwindows, the regularization, the spectroscopic data used and the treatment of horizontal variability of the atmospheric state. Besides the regular data product, a coarse-grid representation of the profiles with unity averaging kernels is available, as well as a specific research product for Middle Atmosphere measurements resulting from a slightly different retrieval approach. The CH_4 errors are dominated by the large spectroscopic uncertainty for line intensities, which probably is too pessimistic, and estimated to be 21 - 34% in the altitude range 6 - 68 km for northern midlatitude summer day conditions. The N_2O errors are 7 - 17% below 45 km. At higher altitudes they increase strongly due to nearly vanishing N_2O amounts. Analysis of the horizontal averaging kernels reveals that for both gases the horizontal resolution is sampling-limited, i.e., information is not smeared over consecutive limb scans. Zonal mean seasonal composites of both CH_4 and N_2O exhibit the typical distribution of source gases with strong upwelling in the tropics and subsidence above the winter poles. Comparison with the previous data version shows several improvements: First, the vertical resolution of the retrieved CH_4 (N_2O) profiles has generally been significantly enhanced and varies between 2.5 (2.5) and 4 (5) km at altitudes between 10 and 60 km, with the best resolution around 30 km for both species. Secondly, the number of not converged retrievals has been clearly reduced, and thirdly, formerly strongly oscillating profiles are now considerably smoother.

1 Introduction

Both methane (CH_4) and nitrous oxide (N_2O) are so-called source gases. That is to say, they are produced on the Earth's surface, and they survive the transport into the stratosphere, since they are chemically quite inert. There, they are decomposed by photolysis and reaction with radicals. N_2O also has an additional source in the upper mesosphere and lower thermosphere (Funke et al., 2008; Sheese et al., 2016; Kelly et al., 2018). The main sink reaction of stratospheric methane is oxidation by the hydroxyl radical OH. Further sink reactions include reaction with excited atomic oxygen ($O(^1D)$), atomic chlorine, and

photolysis. The primary sink reaction of stratospheric nitrous oxide involves $O(^1D)$, but photolysis also plays a role (Brasseur and Solomon, 2005).

Both CH_4 and N_2O act as greenhouse gases. Their global warming potential per molecule exceeds that of CO_2 (Myhre et al., 2014). Beyond this, both species contribute indirectly to stratospheric ozone destruction: Methane is a source of strato-
5 spheric water vapour and thus has impact on the possibility of heterogeneous chemistry via polar stratospheric cloud formation (Shindell, 2001). Nitrous oxide is a source of reactive nitrogen (Ravishankara et al., 2009).

Due to their relatively long stratospheric lifetimes, CH_4 and N_2O are suitable as tracers of stratospheric circulation. Low volume mixing ratios (VMRs) of these species at a given altitude are a sign of a subsided air mass (see, e.g., Toon et al. (1992) or Funke et al. (2014)). Volk et al. (1996) use these gases to analyze lower stratospheric transport, and von Clarmann et al.
10 (2021) use these species to infer middle stratospheric circulation by inversion of the continuity equation.

CH_4 and N_2O can be measured either by air-sampling techniques (e.g., Volk et al., 1996) or by remote sensing. Since any remote observation, whose line of sight runs through the entire atmosphere (ground-based or nadir measurements), is dominated by the tropospheric contribution of these gases, occultation and limb emission measurements are considered as superior to investigate stratospheric dynamics. The list of space missions which have measured one or both of these species includes the
15 Atmospheric Trace Molecule Spectroscopy (ATMOS, Gunson et al. 1996), the Halogen Occultation Experiment (HALOE, Park et al. 1996; Grooß and Russell III 2005), the Atmospheric Chemistry Experiment / Fourier Transform Spectrometer (ACE-FTS, Strong et al. 2008; De Mazière et al. 2008; Sheese et al. 2016), the Microwave Limb Sounder on Aura (Aura-MLS, Lambert et al. 2007; Livesey et al. 2011), the Sub-Millimetre Wave Radiometer on Odin (Odin-SMR, Urban et al. 2005a, b), the Solar Occultation for Ice Experiment (SOFIE, Rong et al. 2016), as well as the SCanning Imaging Absorption spectroMeter
20 for Atmospheric CHartographY (SCIAMACHY, Noël et al. 2016) and the Michelson Interferometer for Passive Atmospheric Sounding (Fischer et al. 2008) on Envisat. A comparison of most of these measurements can be found in Hegglin and Tegtmeier (2017).

Earlier IMK/IAA MIPAS retrievals of CH_4 and N_2O were provided by Glatthor et al. (2005), von Clarmann et al. (2009b), and Plieninger et al. (2015). Bias problems with these data (Laeng et al., 2015; Plieninger et al., 2016) and the availability of
25 MIPAS version 8 spectra triggered the work on a new CH_4 and N_2O data set.

After a brief introduction to the MIPAS instrument (Section 2), we describe the retrieval of CH_4 and N_2O with a strong focus on improvements with respect to preceding data versions (Section 3). In Section 4 the error budget is presented, and vertical as well as horizontal averaging kernels are discussed. Results are presented in Section 5 and discussed in the light of seasonal composites, improved convergence, decreased profile oscillations and comparison with a former validation study (Plieninger
30 et al., 2016). We conclude with a brief discussion of the new data set and identify open problems that could not yet be solved.

2 MIPAS

The Michelson Interferometer for Passive Atmospheric Sounding (MIPAS) was a payload of the Envisat research satellite of the European Space Agency (ESA). Envisat performed 14.4 polar sun-synchronous orbits per day, enabling measurements

with global coverage. MIPAS relied on the measurement technique of mid-infrared Fourier transform spectrometry operating in limb-viewing geometry (Fischer et al., 2008). The spectral coverage was 4.1 to 14.6 μm (685–2410 cm^{-1}). In the first phase of the mission, from June 2002 to March 2004, MIPAS measured at a full spectral resolution (FR) of 0.025 cm^{-1} (unapodized). After a technical defect of the interferometer slide, spectra were recorded in reduced spectral resolution (RR) of 0.0625 cm^{-1}
5 (unapodized) from January 2005 to April 2012.

While the ESA provides their own data product (Dinelli et al., 2021; Raspollini et al., 2022), in this paper recent improvements of the retrieval of CH$_4$ and N$_2$O from MIPAS radiance spectra version 8.03 with the level-2 data processor developed and operated by the Institute for Meteorology and Climate Research (IMK) in cooperation with the Instituto de Astrofísica de Andalucía (IAA) are discussed. Improvements with respect to calibration of the version 8.03 radiance spectra and their
10 relevance to the retrieval are discussed in Kiefer et al. (2021) and Kiefer et al. (2023b). Here we concentrate on the progress made with respect to level-2 processing, i.e., the inference of volume mixing ratios from the radiance spectra and related data characterization.

This paper covers data from both the FR and the RR mission phases and includes measurements recorded in the Nominal (NOM), the Upper Troposphere Lower Stratosphere (UTLS-1), the Middle Atmosphere (MA), the Upper Atmosphere (UA)
15 and the Noctilucent Cloud (NLC) measurement modes. An overview of these modes can be found in the MIPAS mission plan (Oelhaf, 2008). The respective data versions are V8H_CH4_61 and V8H_N2O_61 for FR measurements, V8R_CH4_261 and V8R_N2O_261 for RR NOM measurements, V8R_CH4_161 and V8R_N2O_161 for UTLS-1 measurements, V8R_CH4_662 and V8R_N2O_662 for UA and V8R_CH4_762 and V8R_N2O_762 for NLC measurements. For MA measurements, we offer two co-existing data versions. The versions V8R_CH4_561 and V8R_N2O_561 are more consistent with NOM measurements
20 while V8R_CH4_562 and V8R_N2O_562 are better suited for use in combination with UA measurements (more details in Sect. 3.6). Table 1 gives an overview of the different version 8 CH$_4$ and N$_2$O data products.

3 Retrieval

The retrieval relies on constrained multi-target least squares fitting as described by von Clarmann et al. (2003) and von Clarmann et al. (2009b). The radiative transfer model in use is the Karlsruhe Optimized and Precise Radiative Transfer Algorithm
25 KOPRA (Stiller, 2000). The retrieval of CH$_4$ and N$_2$O is part of a sequential procedure and follows the retrieval of temperature and tangent altitude corrections (Kiefer et al., 2021), ozone (Kiefer et al., 2023b), water vapour (Kiefer et al., 2023a) and HNO$_3$ (Stiller et al., 2023). The results of these preceding V8 retrievals are used for the retrieval of CH$_4$ and N$_2$O. For modelling of the radiance contribution of species, which follow later in the retrieval chain, data version V5 mixing ratios are used.

Both MIPAS IMK/IAA CH$_4$ and N$_2$O profiles always had a high bias in the troposphere and the lower stratosphere with
30 respect to ground-based in-situ measurements and remote measurements in other spectral regions (Laeng et al., 2015; Plieninger et al., 2016). Among other changes, the high methane bias of data versions V5H_CH4_20, V5R_CH4_220 and V5R_CH4_221 was reduced by discarding saturated methane lines, resulting in a remaining bias of the order 0.1–0.2 ppmv. The high bias of V5H_N2O_20, V5R_N2O_220 and V5R_N2O_221 could be lowered to $\sim$20 ppbv (Plieninger et al., 2016). However,

Table 1. List of CH$_4$ and N$_2$O data products. "Retrieval lin/log" indicates retrieval of VMR or of log(VMR).

Mode	Data product	Height range of scan / km	Retrieval lin/log
FR_NOM	CH4_61	6-68	lin
FR_NOM	N2O_61	6-68	lin
RR_NOM	CH4_261	7-72	lin
RR_NOM	N2O_261	7-72	lin
RR_UTLS	CH4_161	5.5-49	lin
RR_UTLS	N2O_161	5.5-49	lin
RR_MA	CH4_561	18-102	lin
RR_MA	N2O_561	18-102	lin
RR_MA	CH4_562	18-102	log
RR_MA	N2O_562	18-102	log
RR_UA	CH4_662	42-112[a]	log
RR_UA	N2O_662	42-112[a]	log
RR_NLC	CH4_762	39-102	log
RR_NLC	N2O_762	39-102	log

(a) Height range used for retrievals. The complete scan of measurements extends up to 172 km.

there was a price to pay in that for resulting data versions V5H_CH4_21, V5H_N2O_21, V5R_CH4_224, V5R_CH4_225, V5R_N2O_224, and V5R_N2O_225, the vertical resolution of both species was considerably deteriorated in the altitude range from 10 to 20 km. The goal of version V8 processing was to improve the vertical resolution relative to version V5 without increasing the high bias again.

5   Another issue with previous data versions was the frequent non-convergence of the retrievals in situations of non-monotonous decrease of CH$_4$ and N$_2$O with altitude or of pronounced horizontal inhomogeneities of the atmospheric state. Such conditions were typically encountered when the line of sight of the measurement passed through the boundary of the polar vortex. In consequence, V8 processing aimed at a higher convergence rate even under extreme atmospheric conditions. In many cases of non-convergence, the target quantities in the course of the iteration flipped back and forth between two solutions, which were

10 associated with approximately the same value of the cost function. In this case, application of an oscillation detection proved to be a particularly useful feature. The oscillation detector calculates the mean of the two solutions as initial guess of the next iteration. More details are given in Kiefer et al. (2021). Beside a second improvement presented in Section 3.1, this intervention led to a considerable decrease of the fraction of not converged retrievals.

    Like for previous CH$_4$- and N$_2$O-retrievals, a more restrictive cloud filter than for temperature and tangent altitude retrieval

15 was used for the V8 data version. As for the temperature and tangent altitude retrieval (Kiefer et al., 2021), a minimum spectral radiance ratio of 4 between analysis windows around 792 and 833 cm^{-1} was required to accept spectra as cloud-free. In addition to this, for CH$_4$ and N$_2$O retrieval spectra were discarded when the ratio of the mean spectral radiances between the analysis windows 1246.3–1249.1 cm^{-1} and 1232.3–1234.4 cm^{-1} was less than 1.8. Due to this more stringent cloud filter,

MIPAS CH_4 and N_2O profiles often do not reach as far down as, e.g., those of temperature, O_3 or HNO_3. Mostly they end at one tangent altitude further above.

The most relevant changes in the V8 retrieval setup compared to the earlier data versions are related to the selection of microwindows, the spectroscopic data, the regularization, the treatment of horizontal variability and the modelling of the zero offset. Some purely technical adjustments resulting in a higher numerical precision of the entire V8 retrieval chain have already been reported by Kiefer et al. (2021) and Kiefer et al. (2023b). In the following we discuss the specific retrieval settings relevant to the combined V8 CH_4 and N_2O retrieval.

3.1 The unknowns of the retrieval

Since CH_4 and N_2O have a lot of overlapping lines, profiles of both species are obtained together in a co-target retrieval. For NOM measurements their profiles are sampled on a discrete retrieval grid with a gridwidth of 1 km between 4 and 70 km and additional levels at 75, 80, 90, 100 and 120 km. For the MA-, UA- and NLC-measurement modes, the retrieval grid also has a 1-km spacing up to 70 km, a 2-km spacing from 70 to 90 km altitude, a 2.5-km spacing between 90 and 95 km, a 5-km spacing between 95 and 110 km, and an additional level at 120 km. In the V8 retrievals, for the first time horizontal mixing ratio gradients of both target gases are additionally retrieved along with the other unknowns (cf. Sect. 3.2). This procedure turned out to be the second essential means to improve the convergence rate. Further, an altitude- and microwindow-dependent background continuum (Sect. 3.1.1), which had proven adequate in previous data versions, as well as a radiance offset correction (Sect. 3.1.2) are retrieved. Contrary to the previous data version, the interfering species H_2O and HNO_3 are no longer joint-fitted along with CH_4 and N_2O, but the profiles of their prior V8 retrievals are used instead. This change saves computation time and has hardly any influence on the retrieved CH_4- and N_2O-profiles. For modelling of O_3 signatures, the previously retrieved V8 profiles are used as well. The interfering species C_2H_2, C_3H_6O (acetone), CFC-113, $ClONO_2$, COF_2, H_2O_2, HCN, HOCl, N_2O_5, NO_2 and SO_2 are modelled by use of the respective V5 profiles, since they are on a later position in the V8 retrieval chain. For modelling of CO_2 and CF_4 climatological profiles are used. The same applies for COF_2, H_2O_2 and HOCl during the period of RR measurements, for which V5 retrievals are not available.

Although some of the microwindows used for CH_4 and N_2O retrieval (cf. Sect. 3.4) contain prominent lines of the water vapour isotopologue HDO, it is not jointly retrieved. Test calculations showed that a joint-fit of HDO mostly led to changes of the order of 1% or less in the lower parts of the CH_4 and N_2O profiles only.

3.1.1 Background continuum

Since the first MIPAS retrievals, a background continuum is fitted to minimize that part of the residual between measured and modeled spectra which cannot be explained by the contribution of trace gas transitions (von Clarmann et al., 2003). This continuum is realized by a wavenumber-independent absorption cross-section per microwindow and altitude. The background continuum has been considered up to the altitude of 58 km since the last data version (for details see Kiefer et al., 2021). Above, the continuum is forced towards zero by a diagonal term of the regularization matrix (cf. Section 3.3). For evaluation

of UTLS-1 measurements the continuum is retrieved for altitudes up to 44 km only, because in this mode the upper end of the limb scan is already at about 50 km altitude.

3.1.2   Radiance offset

To correct for a potentially non-perfect zero-level calibration of the spectra, an additive radiance offset is fitted along with the target variables. The radiance offset correction fitted in previous data versions was allowed to be microwindow dependent, but forced to be altitude-constant. Now it is allowed to be altitude-dependent as well, because Kleinert et al. (2018) have shown that the offset increases with decreasing altitude, which they attribute to straylight from Earth or clouds. Thus, the instrumental performance can be reproduced better by this change. We use a priori information on the offset as provided by Kleinert et al. (2018). This is necessary, because at higher altitudes radiative transfer is close to linear, which makes the background continuum and the radiance offset practically indistinguishable. Without an a priori constraint this would lead to instabilities in the retrieval.

3.2   Horizontal gradients

Traditional limb sounding retrieval methods assume a spherically homogeneous atmosphere where the atmospheric state varies with altitude only. This assumption, however, can be inadequate, and contributed to convergence failures in various previous CH_4 and N_2O retrievals in the vortex boundary region. Ideally, this problem would be solved by a fully tomographic retrieval (see, e.g., Carlotti et al., 2001, 2006; Steck et al., 2005). But in combination with accurate radiative transfer modelling the computational workload involved in this case can be obstructive. Thus, in the V8 retrieval of temperature and line-of-sight a 3D temperature a priori field is scaled to the retrieved profile values, and in addition a horizontal temperature gradient is determined for the upper range of the retrieval altitudes (see Kiefer et al., 2021). This information is used in the CH_4 and N_2O retrievals.

Several approaches to model the horizontal inhomogeneity of the retrieved trace gases - among others of CH_4 and N_2O - were tested as well. One of them was to import the information on the horizontal structure of trace gas fields from previous MIPAS data versions. However, none of the approaches improved the χ^2 of the spectral fit or led to better consistency with the overall 3D structures found in previous data versions. Therefore these approaches were finally discarded. Instead, the horizontal gradients of the CH_4 and N_2O mixing ratios are jointly retrieved along with the mixing ratios, continuum and offset at the nominal geolocation. The fitting of the horizontal CH_4 and N_2O gradients as unknowns is done by including the respective Jacobians in the fitting procedure. These gradients are applied within a range of ± 400 km around the tangent points. No additional assumptions are made. As mentioned above, besides the use of an oscillation detector within the retrieval iterations this treatment also leads to a larger fraction of converged retrievals. A comparison between the V5- and V8-convergence rates is given in Section 5.2.

3.3 Regularization

As usual for IMK/IAA MIPAS data evaluation, the regularization of the V8 methane and nitrous oxide retrieval consists in use of a smoothing term based on a squared first order difference operator (see, e.g., Tikhonov, 1963; Twomey, 1963; Phillips, 1962), for NOM and UTLS1 measurements in combination with a flat all zero a priori profile (for handling of the other modes see Sect. 3.6). In order to avoid large negative mixing ratios at high altitudes an additional diagonal term is included in the regularization matrix, which pushes the result towards the a priori profile. This follows the idea of an optimal estimation or maximum a posteriori retrieval (Rodgers, 2000). This diagonal term is employed at the five highest vertical gridpoints for CH_4 and the two uppermost gridpoints for N_2O only. With this modification, which had already been implemented by Plieninger et al. (2015) for version V5 retrievals, the Tikhonov-type smoothing regularization can be reduced at altitudes above 70 km without risking retrieval instabilities. The formalism to control the altitude dependence of the smoothing constraint used here is described by Kiefer et al. (2021, their Eq. (3)), and replaces the approach by Steck and von Clarmann (2001) that was previously used.

3.4 Microwindows

MIPAS retrievals of CH_4 and N_2O use the spectral region around 1300 cm^{-1} in the MIPAS B-band. The most prominent spectral lines in this region belong to the CH_4 ν_4 band and the N_2O ν_1 band. In comparison to the previous retrieval-setups (V5H_CH4_21, V5H_N2O_21, V5R_CH4_224 and V5R_N2O_224, see Plieninger et al. 2015), the number of spectral gridpoints used for the retrieval of CH_4 and N_2O has been considerably enlarged, both by increasing the wavenumber range used for analysis to 1217.0–1337.9375 cm^{-1} and by taking into account more CH_4 and N_2O lines. Especially the latter change leads to a considerably better altitude resolution in the UTLS region. The new setup consists of 24 microwindows. In order to reduce saturation effects, only microwindows between 1217 and 1260 cm^{-1} are used at tangent altitudes below 16.5 km. Microwindows at higher wavenumbers containing stronger lines are subsequently added at higher tangent altitudes.

The microwindows used for NOminal Mode retrievals (FR and RR) are listed in Table 2. These analysis windows are not always used completely over the full height range. Generally, at lower altitudes spectral gridpoints with appreciable interferences by other species are discarded, depending on the strength of the interference, while at stratospheric altitudes and above the full windows are used. The microwindows applied for MA-, UA- and NLC-retrievals are slightly different in the lower atmosphere.

3.5 Spectroscopy

While former MIPAS level-2 processing relied largely on older spectroscopic data of the HITRAN database (e.g., HITRAN08 for V5 CH_4 and N_2O (Rothman et al., 2009)), for version V8 data processing generally the HITRAN2016 (Gordon et al., 2017) line list was used. In the spectral range of our CH_4 and N_2O retrievals, the HITRAN2016 methane line intensities are only somewhat larger than those of HITRAN2008 - about 1% for weak lines, but clearly below 1% for strong lines. This leads to a very small reduction of up to 0.02 ppmv in retrieved CH_4 mixing ratios. The spectroscopic data for N_2O have hardly changed between HITRAN2008 and HITRAN2016 in the spectral region 1200-1340 cm^{-1}. For O_3 and HNO_3, versions pf3.32 and

Table 2. Microwindows used for MIPAS CH$_4$- and N$_2$O-retrieval for full (first column) and reduced (second column) spectral resolution.

Wavenumber range (FR) (cm^{-1})	Wavenumber range (RR) (cm^{-1})	Altitude range (km)
1217.0000–1221.0500	1217.0000–1221.0625	12–21
1223.5000–1226.5000	1223.5000–1226.5000	12–21
1226.6250–1230.8000	1226.6250–1230.8125	6–72
1231.2500–1235.5000	1231.2500–1235.5000	6–72
1235.7000–1240.0000	1235.6875–1240.0000	6–72
1240.5000–1244.8000	1240.5000–1244.8125	12–72
1245.0000–1249.1250	1245.0000–1249.1250	12–72
1250.3250–1252.8000	1250.3125–1252.8125	6–18
1254.0000–1257.5500	1254.0000–1257.5625	18–72
1258.0000–1259.3000	1258.0000–1259.3125	15–72
1261.3250–1264.1250	1261.3125–1264.1250	18–72
1266.0000–1269.3750	1266.0000–1269.3750	18–72
1270.0000–1274.0000	1270.0000–1274.0000	18–72
1274.3250–1277.5000	1274.3125–1277.5000	18–72
1277.8250–1281.7500	1277.8125–1281.7500	18–72
1282.5000–1283.5500	1282.5000–1283.5625	30–72
1287.6250–1291.6250	1287.6250–1291.6250	30–72
1292.2000–1296.4250	1292.1875–1296.4375	30–72
1296.8750–1299.5000	1296.8750–1299.5000	30–72
1302.7500–1306.5000	1302.7500–1306.5000	30–72
1321.8750–1322.3000	1321.8750–1322.3125	52–72
1326.8750–1327.5000	1326.8750–1327.5000	52–72
1331.8750–1332.9250	1331.8750–1332.9375	52–72
1336.8750–1337.9250	1336.8750–1337.9375	52–72

pf4.45 of the MIPAS spectroscopy were used, respectively. In the latter database, the HNO$_3$ band in the 7.6 μm region is thoroughly adjusted to the band in the 11 μm region, which is essential in order to use the HNO$_3$ prefit.

Although line coupling in the CH$_4$ ν_3 and ν_4 bands has been investigated by Tran et al. (2006), the HITRAN2016 database does not include the relevant data. Thus, line mixing effects are not considered. Resulting retrieval errors are deemed negligible, because Tran et al. (2006) report very small effects in radiance spectra of the CH$_4$ ν_4 band modelled for satellite applications. Beyond this, the effects are largely masked by the signal of interfering species, particularly H$_2$O, N$_2$O, and CO$_2$. The Q-branch, where line-mixing effects are most relevant, is used in our retrieval at altitudes above 28.5 km only. At these low pressures, line mixing is even less of an issue.

3.6 MA, UA and NLC retrieval settings

The retrievals for MA, UA and NLC observation modes differ from those of the NOM measurements with respect to the following settings: The consideration of non-local thermodynamic equilibrium (non-LTE) emissions (López-Puertas and Taylor, 2001), the definition of the state vector, and the regularization chosen.

For CH_4 and N_2O retrievals from measurements recorded in the NOM and UTLS-1 measurement modes, the local thermodynamic equilibrium approximation is adequate. The situation is different for MA, UA, and NLC measurements, where non-LTE emissions of CH_4, N_2O and H_2O have to be considered. Non-LTE populations are computed with the Generic RAdiative traNsfer AnD non-LTE population Algorithm (GRANADA, Funke et al., 2012), which is part of the retrieval iteration in the sense that GRANADA is fed during each iteration with the updated guess values of the relevant atmospheric state variables. For N_2O, the following transitions are considered for non-LTE: 0200-0000, 1000-0000, 0310-0110, 1110-0110, 1200-0200, 1220-0220 and 2000-1000. In retrospective, however, related non-LTE contributions were found to be negligibly small with effects of about 0.1 nW/(cm^{2}sr cm^{-1}). For CH_4, the transitions 0001-0000, 0100-0000, 0002-0001, and 0101-0100 are considered. Only transitions involving the fundamental band were found to show a sizable signal difference associated with non-LTE-effects. The most important non-LTE contributions are associated with the 010-000 and the 020-010 transitions of the interfering species H_2O.

While in NOM, UTLS-1 and the first version of MA retrievals (cf. Sect. 2) the mixing ratios of trace constituents are retrieved, in the second version of MA retrievals (see below) as well as in UA and NLC retrievals their logarithm is retrieved. The effect of this redefinition of the formal state variables is that the regularization is implicitly self-adaptive to the abundance of the species. This turned out to be advantageous because of the large dynamic range of mixing ratios, especially when high altitudes are included. Instead of an all-zero a priori profile as used in the NOM retrievals, gas-dependent a priori profiles are used. For CH_4, these are taken from a climatology generated with the Whole Atmosphere Community Climate Model (WACCM, Marsh, 2011; Marsh et al., 2013) version 4. For N_2O, geolocated output from a specified dynamics WACCM run is used up to the altitude of 90 km. Above 100 km the a priori mixing ratio is set to 20 ppbv, which corresponds to the climatological mean of ACE-FTS profiles (Sheese et al. 2016). Between 90 and 100 km the N_2O a priori is a smooth transition between the WACCM value at 90 km and the climatological mean of 20 ppbv used above 100 km.

For the MA retrievals, we offer two coexisting data versions. Version V8R_CH4_561 and V8R_N2O_561 uses retrieval settings nearly completely consistent with those of the NOM retrievals. The major difference is consideration of non-LTE. Another difference is a slight change of the CH_4 constraint above 70 km altitude. This data version is suggested to be used in combination with NOM measurements, when data users intend to fill gaps in the latter data set with MA data.

Version V8R_CH4_562 and V8R_N2O_562 is better compatible with UA measurements. The main difference to version V8R_CH4_561 and V8R_N2O_561 is that instead of the mixing ratios of the target gases their logarithms are retrieved. Further, only measurements from tangent altitudes at and above 40 km are used. Instead of all zero a prioris, the same a priori profiles as for the UA retrievals are used above 40 km. Like for the UA and NLC retrievals, the constraint has been adjusted

for logarithmic retrievals. Further, a strong diagonal constraint is added to profile values below 35 km altitude in order to tie the results in this altitude range to the V8R_CH4_561 and V8R_N2O_561 data that are used as a priori here.

The additional data product V8R_CH4_562 and V8R_N2O_562 is not meant to supersede the data product V8R_CH4_561 and V8R_N2O_561. Within their diagnostic data (error estimates and averaging kernels) we consider both data versions as valid. As already mentioned above, the data versions 561 are recommended to be used in combination with NOM data and the versions 562 in combination with UA and NLC data.

4 Data characterization

The MIPAS data characterization presented here includes the error budget as well as vertical and horizontal averaging kernel matrices.

4.1 Error budget

Error analysis for both CH_4 and N_2O complies with the recommendations for unified error reporting by von Clarmann et al. (2020) and follows the methodology presented in von Clarmann et al. (2022). Relevant error sources and assumptions on their ingoing uncertainties are compiled in Tables 3 and 4 for FR and RR measurements, respectively. In detail, these tables contain instrumental uncertainties, noise errors from retrieval of temperature, line of sight and prefitted gases, other uncertainties propagated from retrieval of temperature and line of sight and spectroscopic uncertainties. The error ranges for ingoing noise errors were calculated for daytime northern midlatitude summer conditons.

Each error source in our error estimation is assumed to be given as 1-σ uncertainty. However, transformation of the uncertainty intervals of spectroscopic parameters reported in HITRAN2016 into this quantity leaves room for some interpretation. As a reasonable assumption, we decided to regard the average of the lower and upper bound of the intervals reported as 1-σ error bars. If this should turn out to be inadequate, the data user will have to rescale the respective error components of our CH_4 and N_2O profiles.

For estimation of spectroscopic uncertainties, each CH_4 and N_2O line is disturbed in intensity and air-broadened half-width according to its HITRAN error code. For the dominant CH_4 transitions in the analysis windows used here, HITRAN2016 (Gordon et al., 2017) reports error code 3 for line intensity, corresponding to uncertainties larger than 20%. Thus, we perturbed the intensities of the strongest CH_4 lines by 25%. However, the error estimates for these lines are probably too pessimistic, and an error code of 5 (5 – 10%) might be more adequate (I. Gordon, pers. comm., 2023). Application of this error code would lead to considerably lower estimated CH_4 errors. For the air-broadened half-widths error code 6 is reported for strong CH_4 lines, which corresponds to uncertainties between 2% and 5%. Thus, for these lines the air-broadened half-widths are perturbed by 3.5%. For previous MIPAS data versions we used uncertainty estimates by J.-M. Flaud and C. Piccolo (personal communication, 2002), which were much more optimistic with respect to uncertainties in line intensity (2-4% for the strongest CH_4 lines). However, our estimation of uncertainties in air-broadened half-widths was much more conservative then, namely 25%. Interestingly, the combined effect of both ways of disturbing the CH_4 lines leads to approximately the same spectroscopy-

related uncertainty of the retrieved methane mixing ratios in the altitude range up to 30 km. But at higher altitudes our former error estimates led to a much lower spectroscopic error, because the air-broadening becomes more and more unimportant. For strong N_2O lines, HITRAN assigns error code 6 (2-5%) both to line intensities and the air-broadened half-widths. Following our approach this transforms to 1-σ uncertainties of 3.5% used for perturbation of both line parameters.

5   We do not include the smoothing error in the error budget, because it is easily misinterpreted (von Clarmann, 2014). Instead, our CH_4 and N_2O profiles should be conceived as estimates of the smoothed true profile (See Rodgers, 2000, his Section 3.2.1, for a discussion of this concept).

Error profiles representing the effect of measurement noise, provided by the retrievals, are reported separately for each single CH_4 and N_2O profile in the data base. In addition, the data base includes estimates of the total random, total sys-
10   tematic, and total error. These are evaluated for typical atmospheric conditions (northern/southern, polar/midlatitude/tropics, winter/spring/summer/autumn, day/night), and to each CH_4 and N_2O profile the representative error estimates are assigned. In cases of multiplicative error components, the representative error estimates are adjusted to the actual profile. In total, 34 different atmospheric states are taken into account, each of them represented by about 30 geolocations. Following the recommendations of TUNER (Towards Unified Error Reporting, von Clarmann et al., 2020), we categorize each error source either
15   as chiefly random or as chiefly systematic. For mixed errors, which cause both bias and scatter ("headache errors"), both components are reported separately. We aggregate the resulting random and systematic error components separately. The whole set of mean error estimates for each of the different atmospheric conditions is compiled in the Supplement.

As an example, we present the error estimation for daytime northern midlatitude summer. Figure 1 shows height profiles of the total error, total systematic and random errors and of the major single error components as percentage of the mean CH_4
20   and N_2O profiles for this atmospheric scenario. The components "ILS", "spectro" and "gain" are regarded as systematic errors, although the gain error has a small random component as well. The other components are considered as random. The numerical values as well as the respective absolute errors can be found in the Supplement.

The total CH_4 error is rather large and does not vary much over the altitude range 12 to 68 km, namely between 21 and 34% for FR and between 21 and 30% for RR measurements. The reason is the dominance of the spectroscopic error, which nearly
25   accounts for the whole systematic and total error. Consequently, the systematic error is much higher than the random error at altitudes up to 45 km and mostly still twice as high at the altitudes above. The random error is around 4-6% below 40 km and increases up to 15% at higher altitudes. Up to 40 km the noise error accounts for half or more of the random error. At several of the higher altitudes the contribution of the other random errors becomes larger. Other noteworthy error components are the gain error, which around 45 km amounts up to 10% for FR and up to 6% for RR measurements, and the ILS error, which at 45 km
30   is 7% for FR and 5% for RR measurements. However, at most other altitudes these errors are considerably lower. Uncertainties in temperature and line of sight cause an error of 1-3%. The error due to uncertainties in interfering species (H_2O, O_3 and 14 other species) is below 0.4% both for FR and RR measurements and at various altitudes even as low as 0.1%.

Up to 45 km the total N_2O error is 7-17% for FR and 8-16% for RR measurements. At the altitudes above, the error increases strongly: At 56 km it amounts to 45–46%; towards the upper end of the scans it ranges from 73% to more than 100% for the
35   FR mode, and it is completely above 100% for the RR mode. Thus the total N_2O error is clearly lower than the CH_4 error

Table 3. Assumed ingoing uncertainties (FR-NOM): Minimum and maximum ingoing noise errors for temperature, tangent altitude and VMR of interfering species were available from the preceding retrievals of these quantities (northern midlatitude summer day conditions). Minimum and maximum ingoing propagated errors for offset, gain, shift, ILS and CO_2-spectroscopy are taken from the error estimation for temperature and line of sight. Column "Propagation Method": "G" refers to generalized Gaussian error propagation in a matrix formalism, "P" to error estimation via perturbance spectra. The numbers in braces refer to the equation in von Clarmann et al. (2022), in which the respective ingoing error is applied.

Type of Uncertainty	Value/Typical Value[a]	Source	Propagation Method
noise	16 nW/ (cm^2 sr cm^{-1})[b]	Kleinert et al. (2018)	G(16)
offset	2.5 nW/ (cm^2 sr cm^{-1})[b]	Kleinert et al. (2018)	G(5;13)
gain random	0.21%	Kleinert et al. (2018)	P(21;23)
gain systematic	1.03%	Kleinert et al. (2018)	P(21;23)
spectral shift	0.00029 cm^{-1}	V8 retrieval (Kiefer et al., 2021)	P(7)
ILS	3%	Hase (2003)	P(7;14;15)
temperature, noise	0.24 - 1.04 K	V8 retrieval (Kiefer et al., 2021)	G(6)
tangent altitudes, noise	35.0 - 78.5 m	V8 retrieval (Kiefer et al., 2023b)	G(6)
temperature, offset	0.05 - 0.39 K	V8 retrieval (Kiefer et al., 2021)	P(7)
tangent altitudes, offset	8.0 - 23.6 m	V8 retrieval (Kiefer et al., 2023b)	P(7)
temperature, gain systematic	0.30 - 0.79 K	V8 retrieval (Kiefer et al., 2021)	P(19)
tang. alt., gain systemat.	1.9 - 51.1 m	V8 retrieval (Kiefer et al., 2023b)	P(19)
temperature, gain random	0.05 - 0.15 K	V8 retrieval (Kiefer et al., 2021)	P(19)
tang. alt., gain random	0.4 - 9.3 m	V8 retrieval (Kiefer et al., 2023b)	P(19)
temperature, spectral shift	<0.01 - 0.71 K	V8 retrieval (Kiefer et al., 2021)	P(17)
tang. alt., spectral shift	1.6 - 40.8 m	V8 retrieval (Kiefer et al., 2023b)	P(17)
temperature, ILS	0.03 - 1.26 K	V8 retrieval (Kiefer et al., 2021)	P(7)
tangent altitudes, ILS	7.1 - 122.3 m	V8 retrieval (Kiefer et al., 2023b)	P(7)
temperature, CO_2 intens.	0.03 - 0.16 K	V8 retrieval (Kiefer et al., 2021)	P(7)
tang. alt., CO_2 intens.	23.8 - 34.6 m	V8 retrieval (Kiefer et al., 2023b)	P(7)
temperature, CO_2 broad.	0.09 - 1.10 K	V8 retrieval (Kiefer et al., 2021)	P(7)
tang. alt., CO_2 broad.	189.2 - 298.2 m	V8 retrieval (Kiefer et al., 2023b)	P(7)
vmr(H_2O)	1.60×10^{-1} - $2.54\times10^{+0}$ ppmv	V8 retrieval (Kiefer et al., 2023a)	G(6)
vmr(HNO_3)	6.18×10^{-5} - 4.78×10^{-4} ppmv	V8 retrieval (Stiller et al., 2023)	G(6)
vmr(O_3)	3.13×10^{-2} - 1.42×10^{-1} ppmv	V8 retrieval (Kiefer et al., 2023a)	G(6)
vmr(C_2H_2)	2.98×10^{-6} - 1.01×10^{-5} ppmv	V5 retrieval (Glatthor et al., 2007)	G(6)
vmr(C_3H_6O)	4.32×10^{-7} - 8.48×10^{-5} ppmv	V5 retrieval (unpublished data)	G(6)
vmr(CFC-113)	2.17×10^{-7} - 1.21×10^{-5} ppmv	V5 retrieval (unpublished data)	G(6)
vmr($ClONO_2$)	7.29×10^{-6} - 1.02×10^{-4} ppmv	V5 retrieval (von Clarmann et al., 2013)	G(6)
vmr(COF_2)	7.02×10^{-7} - 3.70×10^{-5} ppmv	V5 retrieval (von Clarmann et al., 2012)	G(6)
vmr(H_2O_2)	1.55×10^{-6} - 1.59×10^{-4} ppmv	V5 retrieval (Versick et al., 2012)	G(6)
vmr(HCN)	1.50×10^{-5} - 4.40×10^{-5} ppmv	V5 retrieval (Glatthor et al., 2009)	G(6)
vmr(HOCl)	2.45×10^{-7} - 7.78×10^{-5} ppmv	V5 retrieval (von Clarmann et al., 2012)	G(6)
vmr(N_2O_5)	2.49×10^{-5} - 3.76×10^{-4} ppmv	V5 retrieval (Mengistu Tsidu et al., 2004)	G(6)
vmr(NO_2)	7.78×10^{-8} - 3.78×10^{-4} ppmv	V5 retrieval (Funke et al., 2005)	G(6)
vmr(SO_2)	5.84×10^{-5} - 3.99×10^{-4} ppmv	V5 retrieval (Höpfner et al., 2015)	G(6)
vmr(CO_2)	7.56×10^{-1} - $7.51\times10^{+0}$ ppmv	WACCM model calc. (Kiefer et al., 2021)	P(20)
vmr(CF_4)	5.51×10^{-6} - 1.35×10^{-5} ppmv	database (Kiefer et al., 2002, and updates)	P(7;11)
line intensities CH_4	25%[c]	HITRAN (Gordon et al., 2017)	P(7)
broad. coeff. CH_4	3.5%[c]	HITRAN (Gordon et al., 2017)	P(7)
line intensities N_2O	3.5%[c]	HITRAN (Gordon et al., 2017)	P(7)
broad. coeff. N_2O	3.5%[c]	HITRAN (Gordon et al., 2017)	P(7)

(a) For height dependent uncertainties typical values (min/max) are reported.

(b) unapodized

(c) Uncertainties of the dominant CH_4- and N_2O-lines used for retrieval.

Table 4. Assumed ingoing uncertainties (RR-NOM): For details see Table 3. Ingoing uncertainties for RR-MA- and RR-UA-retrievals are not included in this table, because V5 prefits were not available for these modes, and climatological profiles were used. Maximum ingoing uncertainties for RR-MA- and RR-UA-V8-retrievals of temperature and O_3 at altitudes above 90 km are 7.41 K and 0.28 ppmv, respectively.

Type of Uncertainty	Value/ Typical Value[a]	Source	Propagation Method
noise	10 nW/ (cm^2 sr cm^{-1})[b]	Kleinert et al. (2018)	G(16)
offset	1.5 nW/ (cm^2 sr cm^{-1})[b]	Kleinert et al. (2018)	G(5;13)
gain random	0.21%	Kleinert et al. (2018)	P(21;23)
gain systematic	1.03%	Kleinert et al. (2018)	P(21;23)
spectral shift	0.00029 cm^{-1}	V8 retrieval (Kiefer et al., 2021)	P(7)
ILS	3%	Hase (2003)	P(7;14,15)
temperature, noise	0.22 - 1.23 K	V8 retrieval (Kiefer et al., 2021)	G(6)
tangent altitudes, noise	29.2 - 51.6 m	V8 retrieval (Kiefer et al., 2023b)	G(6)
temperature, offset	0.03 - 0.45 K	V8 retrieval (Kiefer et al., 2021)	P(7)
tangent altitudes, offset	7.5 - 15.5 m	V8 retrieval (Kiefer et al., 2023b)	P(7)
temperature, gain systematic	0.22 - 0.81 K	V8 retrieval (Kiefer et al., 2021)	P(19)
tang. alt., gain systemat.	1.1 - 48.7 m	V8 retrieval (Kiefer et al., 2023b)	P(19)
temperature, gain random	0.04 - 0.15 K	V8 retrieval (Kiefer et al., 2021)	P(19)
tang. alt., gain random	0.2 - 8.9 m	V8 retrieval (Kiefer et al., 2023b)	P(19)
temperature, spectral shift	<0.1 - 0.10 K	V8 retrieval (Kiefer et al., 2021)	P(17)
tang. alt., spectral shift	0.8 - 15.0 m	V8 retrieval (Kiefer et al., 2023b)	P(17)
temperature, ILS	0.05 - 1.16 K	V8 retrieval (Kiefer et al., 2021)	P(7)
tangent altitudes, ILS	7.6 - 113.1 m	V8 retrieval (Kiefer et al., 2023b)	P(7)
temperature, CO_2 intens.	0.03 - 0.18 K	V8 retrieval (Kiefer et al., 2021)	P(7)
tang. alt., CO_2 intens.	26.1 - 34.0 m	V8 retrieval (Kiefer et al., 2023b)	P(7)
temperature, CO_2 broad.	0.14 - 1.47 K	V8 retrieval (Kiefer et al., 2021)	P(7)
tang. alt., CO_2 broad.	198.1 - 251.7 m	V8 retrieval (Kiefer et al., 2023b)	P(7)
vmr(H_2O)	1.87×10^{-1} - $2.24 \times 10^{+0}$ ppmv	V8 retrieval (Kiefer et al., 2023a)	G(6)
vmr(HNO_3)	5.54×10^{-5} - 4.51×10^{-4} ppmv	V8 retrieval (Stiller et al., 2023)	G(6)
vmr(O_3)	2.48×10^{-2} - 8.52×10^{-2} ppmv	V8 retrieval (Kiefer et al., 2023a)	G(6)
vmr(C_2H_2)	3.22×10^{-6} - 9.55×10^{-6} ppmv	V5 retrieval (Glatthor et al., 2007)	G(6)
vmr(C_3H_6O)	5.01×10^{-7} - 8.07×10^{-5} ppmv	V5 retrieval (unpublished data)	G(6)
vmr(CFC-113)	2.26×10^{-7} - 1.14×10^{-5} ppmv	V5 retrieval (unpublished data)	G(6)
vmr($ClONO_2$)	7.38×10^{-6} - 1.04×10^{-4} ppmv	V5 retrieval (von Clarmann et al., 2013)	G(6)
vmr(HCN)	1.54×10^{-5} - 4.41×10^{-5} ppmv	V5 retrieval (Glatthor et al., 2009)	G(6)
vmr(N_2O_5)	2.68×10^{-5} - 3.54×10^{-4} ppmv	V5 retrieval (Mengistu Tsidu et al., 2004)	G(6)
vmr(NO_2)	7.49×10^{-8} - 3.77×10^{-4} ppmv	V5 retrieval (Funke et al., 2005)	G(6)
vmr(SO_2)	5.95×10^{-5} - 4.24×10^{-4} ppmv	V5 retrieval (Höpfner et al., 2015)	G(6)
vmr(CO_2)	7.56×10^{-1} - $7.51 \times 10^{+0}$ ppmv	WACCM model calc. (Kiefer et al., 2021)	P(20)
vmr(CF_4)	5.51×10^{-6} - 1.35×10^{-5} ppmv	database (Kiefer et al., 2002, and updates)	P(7;11)
vmr(COF_2)	6.67×10^{-6} - 6.94×10^{-5} ppmv	database (Kiefer et al., 2002, and updates)	P(7;11)
vmr(H_2O_2)	3.03×10^{-6} - 1.12×10^{-4} ppmv	database (Kiefer et al., 2002, and updates)	P(7;11)
vmr(HOCl)	2.85×10^{-6} - 7.27×10^{-5} ppmv	database (Kiefer et al., 2002, and updates)	P(7;11)
line intensities CH_4	25%[c]	HITRAN (Gordon et al., 2017)	P(7)
broad. coeff. CH_4	3.5%[c]	HITRAN (Gordon et al., 2017)	P(7)
line intensities N_2O	3.5%[c]	HITRAN (Gordon et al., 2017)	P(7)
broad. coeff. N_2O	3.5%[c]	HITRAN (Gordon et al., 2017)	P(7)

(a) For height dependent uncertainties typical values (min/max) are reported.
(b) unapodized
(c) Uncertainties of the dominant CH_4- and N_2O-lines used for retrieval.

at lower altitudes, but considerably higher at the upper altitudes. The reason for the lower relative errors up to 48 km is the smaller spectroscopic uncertainty. At the altitudes above, the N_2O signal becomes very weak, leading to a strong increase of the relative noise error. Consequently, the systematic error exceeds the random error up to about 40 km, while at the altitudes above spectral noise becomes increasingly dominant. The main systematic error components are spectroscopic, gain and ILS

5   errors. Up to 56 km, the spectroscopic error is 4 - 12% for the FR and 4 - 13% for the RR mode, the gain error is 1 - 7% (FR) and 1 - 5% (RR), and the ILS error 0.4 - 7% (FR) and 1 - 5% (RR). At the altitudes above, these errors generally increase strongly. The main random errors are spectral noise and uncertainties in temperature and line of sight. Up to 42 km, spectral noise ranges from 2 to 4% (FR) and from 2 to 7% (RR) and increases strongly above. For both modes the error resulting from uncertainties in temperature and line of sight is 1-2% up to 56 km and somewhat higher above. Up to 56 km the error caused

10   by uncertainties in interfering species is just around 0.1% at various altitudes and 1% at the most. At the uppermost altitudes it increases to 3% for FR and to 18% for RR measurements.

Tangent altitude errors are partly correlated in the altitude domain, random across different limb scans, and fully systematic across different gases. Spectroscopic errors of the target gases are systematic in altitude and in time, except for effects caused by the modulation of the initially systematic errors by variations of the atmospheric state. Gain errors are predominantly

15   systematic in altitude and over one calibration period, but random over longer time periods. ILS errors are chiefly systematic in altitude and time. Errors caused by spectral noise are uncorrelated in time, while the non-diagonal gain matrix of the retrieval causes correlations in the altitude domain.

For the other atmospheric conditions the error estimates show only moderate deviations from the example presented here in the altitude range 12 to 60 km. This applies to NOM measurement mode retrievals as well as to all other measurement modes.

20   Somewhat larger deviations can be found at the upper ends of the scans due to stronger variations in mixing ratios. Further, the errors for MA and UA measurements above 70 km are mostly larger than 100% (cf. Supplement).

4.2   Profile averaging kernels and vertical resolution

Our characterization of the vertical resolution and the content of a priori information of the CH_4 and N_2O profiles relies on the averaging kernel matrices (Rodgers, 2000). Figure 2 shows the averaging kernel rows of CH_4 and N_2O NOM retrievals,

25   respectively, referring to measurements recorded at full spectral resolution at 55.70°N on 10 October 2003 (left column) and at reduced spectral resolution at 41.02°N on 26 December 2009 (right column). In the troposphere and through the whole stratosphere the averaging kernels are well-behaved in the sense that they are fairly symmetric and peak at the nominal altitudes for both modes and gases. However, at higher altitudes they become somewhat asymmetric, and the peaks of the N_2O-AKs are increasingly displaced from their nominal to lower heights.

30   Figure 3 shows the vertical resolution of CH_4 and N_2O profiles in terms of full width at half maximum (FWHM) of the rows of the averaging kernels, obtained with the latest V5- and the V8-retrieval setup. For the measurements at full spectral resolution (left column) the V8 setup has improved in the altitude region 15 to 45 km for CH_4 and between 32 and 42 km for N_2O. Below 15 km, the vertical resolution of N_2O has become slightly worse. Numerically, for the measurements with full spectral resolution the vertical resolution of the V8 CH_4 (N_2O) retrievals varies between 3 (3) and 4.5 (5) km at altitudes

Table 5. Horizontal information distribution for CH$_4$ full resolution (FR) measurements on 29 April 2003 and reduced resolution (RR) measurements on 18 September 2009.

Altitude (km)	FR-Smearing (km)	FR-Displacement (km)	RR-Smearing (km)	RR-Displacement (km)
70	518	-129	598	-26
65	483	-140	521	-46
60	457	-125	374	-66
55	722	72	415	-53
50	524	-91	529	-32
45	657	23	450	-29
40	453	-33	464	-3
35	408	6	376	0
30	356	30	380	35
25	358	72	332	43
20	326	95	292	61
15	292	113	289	89
10	269	131	267	110

between 10 and 50 km. For the measurements at reduced spectral resolution (right column) the V8-setup exhibits a large improvement in the altitude range 10 to 20 km for both gases and above 45 km for N$_2$O. For this mode the vertical resolution obtained with the V8 setup varies between 2.5 (2.5) and 4 (5) km at altitudes between 10 and 65 km, with the best resolution at 30 km altitude for both species.

4.3 Horizontal averaging kernels

Since in limb sounding the line of sight extends over long horizontal distances in the atmosphere, horizontal averaging kernels are an issue. The horizontal averaging kernels are calculated from 2D Jacobians provided by the radiative transfer forward model KOPRA, operated in a 2D mode, for the specified atmosphere. From these 2D Jacobians the 2D averaging kernels are calculated as proposed by von Clarmann et al. (2009a) (their Eq. 5). The way to calculate these 2D averaging kernels thus follows exactly the rationale behind the well-established profile averaging kernels, except that 2D Jacobians are used. Some more information on the technical application of this concept used here can be found in Kiefer et al. (2023b).

We report the horizontal smearing in terms of the full width at half maximum of the horizontal component of the 2D averaging kernels, and the information displacement both for CH$_4$ (Table 5) and N$_2$O (Table 6). The displacement is the horizontal distance between the nominal geolocation of the measurement and the point where most information comes from, calculated as the averaging-kernel-weighted mean horizontal coordinate. The sign convention is such that positive values indicate displacements towards the satellite. The 2D averaging kernels presented here have been calculated for a limb scan, recorded on 29 April 2003 at 47.9°S, 39.8°W, for FR measurements and a limb scan, recorded on 18 September 2009 at 57.1°S, 176.1°W, for RR measurements.

For both gases and the majority of altitudes shown, the horizontal smearing is less than or comparable to the horizontal distance between two subsequent limb scans, which is about 500 km for FR and 400 km for RR measurements. The only

Table 6. Horizontal information distribution for N_2O full resolution (FR) measurements on 29 April 2003 and reduced resolution (RR) measurements on 18 September 2009.

Altitude (km)	FR-Smearing (km)	FR-Displacement (km)	RR-Smearing (km)	RR-Displacement (km)
70	463	-151	493	-62
65	455	-153	471	-66
60	458	-143	428	-72
55	471	-121	357	-66
50	406	-122	344	-59
45	533	-57	352	-48
40	440	-45	374	-29
35	457	9	379	-9
30	383	34	456	69
25	401	77	346	53
20	358	98	310	64
15	357	117	314	89
10	301	125	297	110

exceptions occur at the altitudes around 45 km as well as at the uppermost altitudes. This implies that the horizontal resolution is generally limited by the horizontal sampling of the measurements and not by the horizontal information smearing. Moreover, the information displacement is also fairly small, mostly below 100 km for CH_4 and below 125 km for N_2O, which is well below the horizontal distance between two limb scans. Nevertheless, in atmospheric situations with strong horizontal gradients, like at the boundary of the polar vortices, this displacement might be an issue and should be considered for e.g. comparisons to highly resolving models.

5 Results

5.1 Seasonal composites

In Figures 4 and 5 we show zonal mean seasonal composites of CH_4 and N_2O retrieved in the NOM HR and NOM RR modes (V8H_CH4_61, V8R_CH4_161, V8R_CH4_261, V8H_N2O_61, V8R_N2O_161, V8R_N2O_261) during the period 2002-2012. Both distributions exhibit the typical features of a tropospheric trace gas with maximum VMRs in the troposphere, strong upwelling in the tropics with sharp latitudinal gradients at $\pm 20°$ in the lower to mid-stratosphere (so-called tropical pipe, (Plumb, 1996)), and downwelling above the winter poles. The tropospheric VMRs are somewhat higher between 40°S and 40°N than at higher latitudes, namely by 0.1-0.2 ppmv for CH_4 and by 20-30 ppbv for N_2O.

The upwelling in the tropical lower to mid-stratosphere exhibits slight latitudinal asymmetries characterized by a "nose" in the 1.6 ppmv contourline of CH_4, which, e.g., during boreal and austral summer indicates transport towards the respective winter hemisphere. At higher altitudes there are larger-scale seasonal differences. During March to May, a double-peak is visible at 40-50 km with maxima at 30°S and 30°N and a local minimum at the Equator. This feature has already been detected

in CH_4 measurements of the Stratospheric And Mesospheric Sounder (SAMS) from 1979 on the NIMBUS 7 satellite (Jones and Pyle, 1984). The sharp meridional gradient in stratospheric CH_4 around 60°S, with very low VMRs extending much further down than at northern high latitudes, reflects the beginning formation of the Antarctic vortex. During June to August the southern tropical peak above 40 km has disappeared both for CH_4 and N_2O and is replaced by a kind of shoulder in the altitude range 30-40 km. Just below, the weak vertical and meridional gradient, identifiable e.g. from the wide distance between the 1.4 and 1.2 ppmv methane isolines, marks the formation of a pronounced surf zone in the southern winter-hemisphere. In contrast, the northern peak has expanded even more upwards showing the beginning formation of the Brewer-Dobson cell of the next northern winter. Caused by progressed subsidence in the Antarctic vortex, low CH_4 and N_2O VMRs have subsided further downward at high southern latitudes. During September to November the northern tropical maximum is at somewhat lower altitudes than during summer. In the altitude range of 30-40 km there is a moderate southward decline of the contourlines up to the edge of the Antarctic vortex at 70°S, which still exists below 30 km. In the upper stratosphere the Antarctic vortex has largely been replaced by midlatitude airmasses. In the northern hemisphere the beginning build-up of the Arctic vortex is visible in the upper stratosphere. The period December to February has several similarities to June to August, if mirrored at the Equator. Above 40 km there is a maximum at 20°S, but not quite as distinct as the northern tropical maximum during boreal summer. The Arctic vortex reflects progressed subsidence, but not as strong as its southern hemispheric counterpart during June to August.

5.2 Major improvements with respect to preceding versions

To illustrate improvements achieved with respect to convergence failures and profile oscillations we compare latitude-height cross sections of CH_4 data versions V5R_CH4_224 and V8R_CH4_261 for two selected orbits (Figure 6). The top row shows the CH_4 distribution along orbit 29041 of 19 September 2007. With the old setup, convergence was not achieved for seven scans through the Antarctic vortex marked by white vertical stripes (top left). However, due to the use of the oscillation detector and modelling of horizontal CH_4 and N_2O gradients the number of not converged scans is reduced to just one with the V8-retrieval setup (top right). In general, this treatment leads to a much larger fraction of converged retrievals. For FR measurements, the portion of non-converged retrievals is reduced from 8.4% to 0.3%. For RR measurements, this number is lowered from 0.36% to 0.10%. While for RR measurements the fraction of non-converged retrievals had also been rather low for the previous dataset, it has to be considered that these - like in our example - were not randomly distributed but associated with situations characterized by large horizontal inhomogeneities, such as vortex boundary conditions, where they cause sizable data gaps. Hence, this reduction in non-converged profiles is a significant improvement.

The use of horizontal CH_4 and N_2O gradients also leads to smoother profiles at geolocations, where formerly retrieved profiles had been strongly oscillating. This, e.g., can be seen in the CH_4 distributions along orbit 30832 of 23 January 2008 (bottom row). For this orbit, retrievals are especially complicated at the edge of the inclined arctic vortex around 70°N, where vertical profiles have local maxima around 30 km. In this region the dataset V5R_CH4_N2O_224 exhibits strong oscillations (bottom left), which have disappeared in the V8 data (bottom right). For a more detailed picture, Figure 7 shows single CH_4

profiles for two scans in this critical region. While the V5R-profiles are strongly oscillating between 20 and 30 km with unphysically high vertical frequency, the V8R-profiles are much smoother in this height region.

5.3 Delta-validation

The previous CH_4 and N_2O datasets were extensively validated by comparison with other satellite data and groundbased measurements (Plieninger et al., 2016). The outcome of this validation was that, below 25 km, there was likely a positive bias against other satellite measurements: 0.1 to 0.2 ppmv for CH_4 and up to 30 ppbv for N_2O. To check if the positive bias is still present in the V8 datasets, we limit ourselves to a delta-validation against the preceding dataset. That ist to say, instead of validating the new data product from the scratch, we analyze the degree to which issues identified in Plieninger et al. (2016) are removed or increased in the new data product.

Figure 8 (top) shows zonal mean differences between V8 and V5 CH_4, averaged over the full resolution period (left) and the reduced resolution period (right). We abstain from presenting seasonal composites, because apart from the Antarctic region the differences are rather similar in every season. The deviations between the FR data consist of oscillations of up to ±0.15 ppmv in the altitude range of 5–40 km and smaller oscillations above. The positive differences at 30 km apparently increase the bias between V5 data and validation experiments at this altitude shown by Plieninger et al. (2016) (their Figs. 9, 10, 11), while the negative differences at 40 km have the opposite effect. At lower altitudes, a delta-validation becomes more ambiguous, because the V8-V5 differences are latitude dependent. At 20 km they are negative at low latitudes and positive at high northern latitudes, but at 10 km it is the opposite. Thus, at 20 km there seems to be a better agreement to the validation experiments in the tropics and a deterioration in the northern extra-tropics, but at 10 km it looks the other way round. Except for the lowermost altitudes, the differences at high southern latitudes are mostly negative up to the altitude of 40 km, which generally tends to improve the agreement to validation experiments.

The CH_4 differences of the RR period (top right) show some similar features as those of the FR period, namely negative values at 40 km and positive values at 30 km. However, there are also clear deviations: First, a much broader band of positive differences at the lower end of the latitudinal cross section as well as positive values between 10 and 20 km, extending from the tropics towards mid-latitudes. Second, there is better agreement at high southern latitudes above 20 km. The positive differences below 20 km lead to an increase of the high bias of $\sim$0.15 ppmv in this altitude region shown in Plieninger et al. (2016) by about 0.1 ppmv. The negative difference between 35 and 45 km compensates a slight positive bias in the previous CH_4 dataset. The positive bias above 65 km is due to a deficiency in the V5 data, which exhibit a kink in the profile shape at this altitude. In summary the CH_4 bias at all altitudes is well below the total error presented in Sect. 4.1.

The V8-V5 differences in N_2O of the FR period (bottom left) are spatially well correlated with those of CH_4. Slight deviations are a small downward shift of the mid-stratospheric positive differences to 27 km and restriction to the tropics. The negative differences at 10 km lead to a reduction of the high bias of the V5 data at this altitude against ACE-FTS (Plieninger et al., 2016), their Fig. 13) by $\sim$15 ppbv. The small negative differences just below 20 km and the positive differences around 27 km apparently also reduce the bias against ACE-FTS, while the positive V8-V5 differences at 20 km rather lead to an increased bias.

The main differences between V8 and V5 N_2O of the RR period (bottom right) are a nearly global band of up to 20 ppbv oscillating between 10 and 20 km and a region of up to 15 ppbv at tropical and mid-latitudes around 27 km. The negative differences at 10 km are much weaker than for the FR period. There are also some spatial correlations with the V8-V5 differences in CH_4 of the RR period. Generally, the positive V8-V5 differences lead to an enhancement of the high bias against ACE-FTS and MLS as presented in Plieninger et al. (2016) for the altitude region below 30 km. At the altitudes of 10 km in the tropics this might cause an increase of the bias against ACE-FTS from 25 to 40 ppbv. This bias is larger than the total N_2O error presented in Sect. 4.1 for the lowermost altitudes.

Since there is a generally good consistency between V5 data of the FR and RR period both for CH_4 and N_2O, the deviations between the left-hand and the right-hand plots in Figure 8, especially in the lower atmosphere, indicate an offset between the V8 data of the two periods. The deviations are largest at high latitudes around 10 km and in the tropics around 15 km, with CH_4 differences between RR and FR data of 10-15% and of 5%, respectively. For N_2O, the respective RR-FR differences are 7% and 2%. However, at higher altitudes the consistency between V8 RR and FR data is good.

5.4 Coarse grid results

Quantitative application of the standard CH_4 and N_2O results obtained from regularized retrievals requires educated data users, who are familiar with the averaging kernel formalism. In order to make the use of MIPAS data within comparisons to model data easier, we provide an alternative representation on a coarser vertical grid of 23 pressure levels: 1000, 700, 400, 250, 150, 100, 50, 30, 15, 10, 5, 3, 1.5, 1, 0.5, 0.3, 0.1, 0.03, 0.01, 0.003, 0.001, 0.0003, and 0.00003 hPa. These values are a subset of a grid often used by chemistry-climate modellers (Eyring et al., 2013). In this representation, all information on the vertical resolution is included in the vertical grid, and no averaging kernels need to be considered (von Clarmann et al., 2015). These data are generated by maximum likelihood retrievals on a vertical grid coarse enough that effectively no regularization is required. The averaging kernels associated with these retrievals are unity by definition. Contrary to the standard retrievals which represent mixing ratios at levels, and where linear variation in altitude is assumed between the levels, the coarse grid data are given as mean layer values. The boundaries of these layers are defined by pressure values, and the grid is constant for the entire data set. This makes interpolation unnecessary and simplifies comparison with model results or time series analysis.

In Figure 9 we compare the results of the standard (left) and of the coarse grid retrieval (right) for orbit 30863 from 25 January 2008. The main spatial features detected in the standard retrieval are also resolved in the coarse grid retrieval for CH_4 (top row) as well as for N_2O (bottom row). However, due to the coarser vertical grid, very fine spatial structures become blurry. This, e.g., becomes apparent in the CH_4 distribution at and above 30 km (10 hPa) in the region of the arctic vortex north of 60°N.

6 Conclusions

We presented MIPAS IMK/IAA methane and nitrous oxide data based on the most recent version 8 level-1b spectra and processed using an improved retrieval approach. After description of the new retrieval setup, we performed a comprehensive

error assessment considering the formalism outlined in the TUNER report (von Clarmann et al., 2020). Due to the large uncertainties in line intensity given in HITRAN2016 - which probably are too pessimistic - the total CH_4 error is between 21 and 34% in the altitude range 6 - 68 km for the atmospheric scenario presented (northern midlatitude summer day). For the same atmospheric conditions, the total N_2O error grows from 7% at 12 km to 17% at 45 km. At the altitudes above the error increases strongly due to very low N_2O signatures. We consider MIPAS version V8 CH_4 and N_2O data versions as superior over preceding versions. The main reasons are the following:

- The data are based on better calibrated level-1B spectra. In particular, trends are supposed to be less affected by instrumental drifts.

- The vertical resolution generally is better than that of the preceding version. This has been achieved by use of more CH_4 and N_2O lines in the retrieval setup.

- The fraction of converged retrievals has been increased. This has been achieved by application of an oscillation detector within the iterations of the retrieval and by additional retrieval of horizontal CH_4 and N_2O gradients. In particular, in situations where the line of sight crossed the boundary of the polar vortex, i.e. where, due to polar subsidence, very different mixing ratios were encountered at the same altitude in front of and behind the tangent point, non-consideration of the oscillation detector and of horizontal gradients had prevented retrievals from converging.

However, below 10 km the V8_CH4_261 retrievals at all latitudes result in up to 0.1 ppmv higher volume mixing ratios than the already high biased V5 data. The same applies for the altitude regions around 15 km and 25–30 km at low and mid-latitudes. On the other hand the agreement with validation experiments seems to be improved at 20 and 40 km. For V8_CH4_61 retrievals the positive differences to the V5 data below 10 km and around 15 km are less pronounced. For V8R_N2O_261 retrievals the high bias in V5 N_2O is increased by up to 20 ppbv in a nearly global band oscillating between 10 and 20 km altitude and by up to 15 ppbv at low latitudes around 27 km. For V8H_N2O_61 retrievals the increase of the bias in these regions is clearly less distinct. Further, the negative differences between the FR data at 10 km reduce the high bias in V5 N_2O found at this altitude.

We suspect that the high bias of both gases to a large part might be due to the spectroscopic data used, which suffer from large uncertainties. The high bias of N_2O presumably has additional yet unidentified causes, since it clearly exceeds the reported spectroscopic uncertainties. Further, we attribute the observed oscillations in the V8-V5 differences, which are partly correlated between CH_4 and N_2O, to the better vertical resolution in V8 profiles.

The problem of uncertain spectroscopic data is not so severe in the case of ground-based and a couple of space-borne instruments that measure CH4 in solar absorption using the ν_3 band near 3000 cm^{-1}. A lot of work went into improving the accuracy of the spectroscopic data in that region. Emission spectroscopy, however, has to use longer wavelengths where the Planck function at terrestrial temperatures has values, which are high enough to provide a sufficiently large signal. We urge the spectroscopic community to devote a similar effort to the ν_4 region to improve satellite measurements of CH_4 by emission instruments.

References

Brasseur, G. and Solomon, S.: Aeronomy of the Middle Atmosphere–Chemistry and Physics of the Stratosphere and Mesosphere, Atmospheric and Oceanographic Sciences Library 32, Springer, P. O. Box 17, 3300 AA Dordrecht, The Netherlands, ISBN 978-1-4020-3284-4, doi:10.1007/1-4020-3824-0, third edn., https://doi.org/10.1007/1-4020-3824-0, 2005.

5 Carlotti, M., Dinelli, B. M., Raspollini, P., and Ridolfi, M.: Geo–fit approach to the analysis of limb–scanning satellite measurements, Appl. Opt., 40, 1872–1885, https://doi.org/10.1364/AO.40.001872, https://opg.optica.org/ao/abstract.cfm?URI=ao-40-12-1872, 2001.

Carlotti, M., Brizzi, G., Papandrea, E., Prevedelli, M., Ridolfi, M., Dinelli, B. M., and Magnani, L.: GMTR: Two–dimensional geo–fit multitarget retrieval model for Michelson Interferometer for Passive Atmospheric Sounding/Environmental Satellite observations, Appl. Opt., 45, 716–727, https://doi.org/10.1364/AO.45.000716, https://opg.optica.org/ao/abstract.cfm?URI=ao-45-4-716, 2006.

10 De Mazière, M., Vigouroux, C., Bernath, P. F., Baron, P., Blumenstock, T., Boone, C., Brogniez, C., Catoire, V., Coffey, M., Duchatelet, P., Griffith, D., Hannigan, J., Kasai, Y., Kramer, I., Jones, N., Mahieu, E., Manney, G. L., Piccolo, C., Randall, C., Robert, C., Senten, C., Strong, K., Taylor, J., Tétard, C., Walker, K. A., and Wood, S.: Validation of ACE–FTS v2.2 methane profiles from the upper troposphere to lower mesosphere, Atmos. Chem. Phys., 8, 2421–2435, https://doi.org/10.5194/acp-8-2421-2008, 2008.

Dinelli, B. M., Raspollini, P., Gai, M., Sgheri, L., Ridolfi, M., Ceccherini, S., Barbara, F., Zoppetti, N., Castelli, E., Papandrea, E., Pettinari, P., Dehn, A., Dudhia, A., Kiefer, M., Piro, A., Flaud, J.-M., López-Puertas, M., Moore, D., Remedios, J., and Bianchini, M.: The ESA MIPAS/ENVISAT level2-v8 dataset: 10 years of measurements retrieved with ORM v8.22, Atmos. Meas. Tech., 14, 7975–7998, https://doi.org/10.5194/amt-14-7975-2021, 2021.

Eyring, V., Lamarque, J.-F., Hess, P., Arfeuille, F., Bowman, K., Chipperfield, M. P., Duncan, B., Fiore, A., Gettelman, A., Giorgetta, M. A., Granier, C., Hegglin, M., Kinnison, D., Kunze, M., Langematz, U., Luo, B., Martin, R., Matthes, K., Newman, P. A., Peter, T., Robock, A.,
20 Ryerson, T., Saiz-Lopez, A., Salawitch, R., Schultz, M., Shepherd, T. G., Shindell, D., Staehelin, J., Tegtmeier, S., Thomason, L., Tilmes, S., Vernier, J.-P., Waugh, D. W., and Young, P. J.: Overview of IGAC/SPARC Chemistry–Climate Model Initiative (CCMI) Community Simulations in Support of Upcoming Ozone and Climate Assessments, SPARC Newsletter, 40, 48–66, https://www.sparc-climate.org/wp-content/uploads/sites/5/2017/12/SPARCnewsletter_No40_Jan2013_web.pdf, 2013.

Fischer, H., Birk, M., Blom, C., Carli, B., Carlotti, M., von Clarmann, T., Delbouille, L., Dudhia, A., Ehhalt, D., Endemann, M., Flaud,
25 J. M., Gessner, R., Kleinert, A., Koopmann, R., Langen, J., López-Puertas, M., Mosner, P., Nett, H., Oelhaf, H., Perron, G., Remedios, J., Ridolfi, M., Stiller, G., and Zander, R.: MIPAS: an instrument for atmospheric and climate research, Atmos. Chem. Phys., 8, 2151–2188, https://doi.org/10.5194/acp-8-2151-2008, 2008.

Funke, B., López-Puertas, M., von Clarmann, T., Stiller, G. P., Fischer, H., Glatthor, N., Grabowski, U., Höpfner, M., Kellmann, S., Kiefer, M., Linden, A., Mengistu Tsidu, G., Milz, M., Steck, T., and Wang, D. Y.: Retrieval of stratospheric NO_x from 5.3 and 6.2 μm nonlocal
30 thermodynamic equilibrium emissions measured by Michelson Interferometer for Passive Atmospheric Sounding (MIPAS) on Envisat, J. Geophys. Res., 110, D09302, https://doi.org/10.1029/2004JD005225, 2005.

Funke, B., García-Comas, M., López-Puertas, M., Glatthor, N., Stiller, G. P., von Clarmann, T., Semeniuk, K., and McConnell, J. C.: Enhancement of N_2O during the October-November 2003 solar proton event, Atmos. Chem. Phys., 8, 3805–3815, https://doi.org/10.5194/acp-8-3805-2008, https://acp.copernicus.org/articles/8/3805/2008/, 2008.

35 Funke, B., López-Puertas, M., García-Comas, M., Kaufmann, M., Höpfner, M., and Stiller, G. P.: GRANADA: A Generic RAdiative traNsfer AnD non-LTE population algorithm, J. Quant. Spectrosc. Radiat. Transfer, 113, 1771–1817, https://doi.org/10.1016/j.jqsrt.2012.05.001, 2012.

Funke, B., López-Puertas, M., Stiller, G. P., and von Clarmann, T.: Mesospheric and stratospheric NOy produced by energetic particle precipitation during 2002-2012, J. Geophys. Res. Atmos., 119, 4429–4446, https://doi.org/10.1002/2013JD021404, 2014.

Glatthor, N., von Clarmann, T., Fischer, H., Funke, B., Grabowski, U., Höpfner, M., Kellmann, S., Kiefer, M., Linden, A., Milz, M., Steck, T., Stiller, G. P., Mengistu Tsidu, G., and Wang, D. Y.: Mixing processes during the Antarctic vortex split in September/October 2002 as inferred from source gas and ozone distributions from ENVISAT-MIPAS, J. Atmos. Sci., 62, 787–800, https://doi.org/10.5194/acp-8-3805-2008, https://acp.copernicus.org/articles/8/3805/2008/, 2005.

Glatthor, N., von Clarmann, T., Fischer, H., Funke, B., Grabowski, U., Höpfner, M., Kellmann, S., Linden, A., Milz, M., Steck, T., and Stiller, G. P.: Global peroxyacetyl nitrate (PAN) retrieval in the upper troposphere from limb emission spectra of the Michelson Interferometer for Passive Atmospheric Sounding (MIPAS), Atmospheric Chemistry and Physics, 7, 2775–2787, https://doi.org/10.5194/acp-7-2775-2007, https://acp.copernicus.org/articles/7/2775/2007/, 2007.

Glatthor, N., von Clarmann, T., Stiller, G. P., Funke, B., Koukouli, M. E., Fischer, H., Grabowski, U., Höpfner, M., Kellmann, S., and Linden, A.: Large-scale upper tropospheric pollution observed by MIPAS HCN and C_2H_6 global distributions, Atmos. Chem. Phys., 9, 9619–9634, https://doi.org/10.5194/acp-9-9619-2009, https://acp.copernicus.org/articles/9/9619/2009/, 2009.

Gordon, I. E., Rothman, L. S., Hill, C., Kochanov, R. V., Tan, Y., Bernath, P. F., Birk, M., Boudon, V., Campargue, A., Chance, K. V., Drouin, B. J., Flaud, J.-M., Gamache, R. R., Hodges, J. T., Jacquemart, D., Perevalov, V. I., Perrin, A., Shine, K. P., Smith, M.-A. H., Tennyson, J., Toon, G. C., Tran, H., Tyuterev, V. G., Barbe, A., Császár, A. G., Devi, V. M., Furtenbacher, T., Harrison, J. J., Hartmann, J.-M., Jolly, A., Johnson, T. J., Karman, T., Kleiner, I., Kyuberis, A. A., Loos, J., Lyulin, O. M., Massie, S. T., Mikhailenko, S. N., Moazzen-Ahmadi, N., Müller, H. S. P., Naumenko, O. V., Nikitin, A. V., Polyansky, O. L., Rey, M., Rotger, M., Sharpe, S. W., Sung, K., Starikova, E., Tashkun, S. A., Vander Auwera, J., Wagner, G., Wilzewski, J., Wcisło, P., Yu, S., and Zak, E. J.: The HITRAN2016 molecular spectroscopic database, J. Quant. Spectrosc. Radiat. Transfer, 203, 3–69, https://doi.org/10.1016/j.jqsrt.2017.06.038, 2017.

Grooß, J.-U. and Russell III, J. M.: Technical note: A stratospheric climatology for O_3, H_2O, CH_4, NO_x, HCl and HF derived from HALOE measurements, Atmos. Chem. Phys., 5, 2797–2807, https://doi.org/10.5194/acp-6-2767-2006, 2005.

Gunson, M. R., Abbas, M. M., Abrams, M. C., Allen, M., Brown, L. R., Brown, T. L., Chang, A. Y., Goldman, A., Irion, F. W., Lowes, L. L., Mahieu, E., Manney, G. L., Michelsen, H. A., Newchurch, M. J., Rinsland, C. P., Salawitch, R. J., Stiller, G. P., Toon, G. C., Yung, Y. L., and Zander, R.: The Atmospheric Trace Molecule Spectroscopy (ATMOS) experiment: Deployment on the ATLAS Space Shuttle missions, Geophys. Res. Lett., 23, 2333–2336, https://doi.org/https://doi.org/10.1029/96GL01569, https://agupubs.onlinelibrary.wiley.com/doi/abs/10.1029/96GL01569, 1996.

Hase, F.: The instrument line shape of MIPAS, Oral presentation at the 2nd MIPAS Quality Working Group Meeting, Florence, 3 Dec. 2003, 2003.

Hegglin, M. I. and Tegtmeier, S., eds.: The SPARC Data Initiative: Assessment of stratospheric trace gas and aerosol climatologies from satellite limb sounders, SPARC Report No. 8, WCRP-5/2017, SPARC, https://doi.org/10.3929/ethz-a-010863911, 2017.

Höpfner, M., Boone, C. D., Funke, B., Glatthor, N., Grabowski, U., Günther, A., Kellmann, S., Kiefer, M., Linden, A., Lossow, S., Pumphrey, H. C., Read, W. G., Roiger, A., Stiller, G., Schlager, H., von Clarmann, T., and Wissmüller, K.: Sulfur dioxide (SO_2) from MIPAS in the upper troposphere and lower stratosphere 2002-2012, Atmos. Chem. Phys., 15, 7017–7037, https://doi.org/10.5194/acp-15-7017-2015, 2015.

Jones, R. L. and Pyle, J. A.: Observations of CH_4 and N_2O by the NIMBUS 7 SAMS: A comparison with in situ data and two-dimensional numerical model calculations, J. Geophys. Res., 89, 5263–5279, https://doi.org/10.1029/JD089iD04p05263, 1984.

Kelly, K. K., Chipperfield, M. P., Plane, J. M. C., Feng, W., Sheese, P. E., Walker, K. A., and Boone, C. D.: An Explanation for the Nitrous Oxide Layer Observed in the Mesopause Region, Geophys. Res. Lett., 45, 7818–7827, https://doi.org/https://doi.org/10.1029/2018GL078895, https://agupubs.onlinelibrary.wiley.com/doi/abs/10.1029/2018GL078895, 2018.

Kiefer, M., von Clarmann, T., and Grabowski, U.: State parameter Data Base for MIPAS Data Analysis, Adv. Space Res., 30, 2387–2392,
5   https://doi.org/https://doi.org/10.1016/S0273-1177(02)80284-8, https://www.sciencedirect.com/science/article/pii/S0273117702802848, 2002.

Kiefer, M., von Clarmann, T., Funke, B., García-Comas, M., Glatthor, N., Grabowski, U., Kellmann, S., Kleinert, A., Laeng, A., Linden, A., López-Puertas, M., Marsh, D., and Stiller, G. P.: IMK/IAA MIPAS temperature retrieval version 8: nominal measurements, Atmos. Meas. Tech., 14, 4111–4138, https://doi.org/10.5194/amt-14-4111-2021, 2021.

10 Kiefer, M., Glatthor, N., Stiller, G. P., von Clarmann, T., Funke, B., Grabowski, U., Kellmann, S., and Linden, A.: H₂O paper, paper in preparation, 2023a.

Kiefer, M., von Clarmann, T., Funke, B., García-Comas, M., Glatthor, N., Grabowski, U., Höpfner, M., Kellmann, S., Laeng, A., Linden, A., López-Puertas, M., and Stiller, G. P.: Version 8 IMK/IAA MIPAS ozone profiles: nominal observation mode, Atmos. Meas. Tech., 16, 1443–1460, https://doi.org/10.5194/amt-16-1443-2023, https://amt.copernicus.org/articles/16/1443/2023/, 2023b.

15 Kleinert, A., Birk, M., Perron, G., and Wagner, G.: Level 1b error budget for MIPAS on ENVISAT, Atmos. Meas. Tech., 11, 5657–5672, https://doi.org/10.5194/amt-11-5657-2018, 2018.

Laeng, A., Plieninger, J., von Clarmann, T., Grabowski, U., Stiller, G., Eckert, E., Glatthor, N., Haenel, F., Kellmann, S., Kiefer, M., Linden, A., Lossow, S., Deaver, L., Engel, A., Hervig, M., Levin, I., McHugh, M., Noël, S., Toon, G., and Walker, K.: Validation of MIPAS IMK/IAA methane profiles, Atmos. Meas. Tech., 8, 5251–5261, https://doi.org/10.5194/amt-8-5251-2015, 2015.

20 Lambert, A., Read, W. G., Livesey, N. J., Santee, M. L., Manney, G. L., Froidevaux, L., Wu, D. L., Schwartz, M. J., Pumphrey, H. C., Jimenez, C., Nedoluha, G. E., Cofield, R. E., Cuddy, D. T., Daffer, W. H., Drouin, B. J., Fuller, R. A., Jarnot, R. F., Knosp, B. W., Pickett, H. M., Perun, V. S., Snyder, W. V., Stek, P. C., Thurstans, R. P., Wagner, P. A., Waters, J. W., Jucks, K. W., Toon, G. C., Stachnik, R. A., Bernath, P. F., Boone, C. D., Walker, K. A., Urban, J., Murtagh, D., Elkins, J. W., and Atlas, E.: Validation of the Aura Microwave Limb Sounder middle atmosphere water vapor and nitrous oxide measurements, J. Geophys. Res., 112, D24S36, https://doi.org/10.1029/2007JD008724,
25 2007.

Livesey, N. J., Read, W. G., Froidevaux, L., Lambert, A., Manney, G. L., Pumphrey, H. C., Santee, M. L., Schwartz, M. J., Wang, S., Cofeld, R. E., Cuddy, D. T., Fuller, R. A., Jarnot, R. F., Jiang, J. H., Knosp, B. W., Stek, P. C., Wagner, P. A., and Wu., D. L.: EOS MLS Version 3.3 Level 2 data quality and description document, Tech. rep., Jet Propulsion Laboratory, https://mls.jpl.nasa.gov/data/v3-3_data_quality_document.pdf, d-33509, available from https://mls.jpl.nasa.gov/data/v3-3_data_quality_document.pdf, 2011.

30 López-Puertas, M. and Taylor, F. W.: Non-LTE Radiative Transfer in the Atmosphere, doi:10.1142/4650, World Scientific Pub., Singapore, https://doi.org/10.1142/4650, 2001.

Marsh, D. R.: Chemical-dynamical coupling in the mesosphere and lower thermosphere, in: Aeronomy of the Earth's atmosphere and ionosphere, edited by Abdu, M. A. and Pancheva, D., vol. 2 of *IAGA Special Sopron Book*, pp. 3–17, doi:10.1007/978-94-007-0326-1, ISBN: 978-94-007-0326-1, Springer, Dordrecht, 1st edn., 2011.

35 Marsh, D. R., Mills, M. J., Kinnison, D. E., Lamarque, J.-F., Calvo, N., and Polvani, L. M.: Climate change from 1850 to 2005 simulated in CESM1(WACCM), J. Clim., 26, 7372–7391, https://doi.org/10.1175/JCLI-D-12-00558.1, 2013.

Mengistu Tsidu, G., von Clarmann, T., Stiller, G. P., Höpfner, M., Fischer, H., Glatthor, N., Grabowski, U., Kellmann, S., Kiefer, M., Linden, A., Milz, M., Steck, T., Wang, D.-Y., and Funke, B.: Stratospheric N₂O₅ in the austral spring 2002 as retrieved from limb
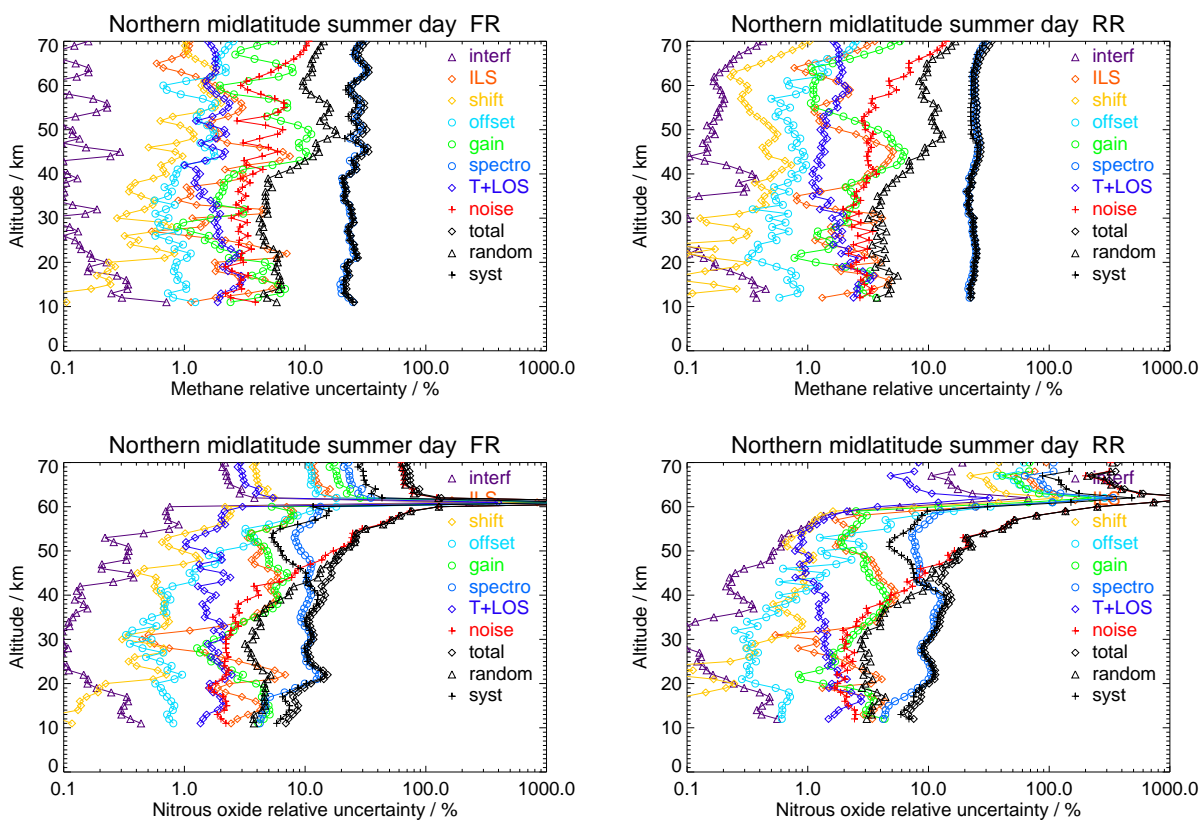
emission spectra recorded by the Michelson Interferometer for Passive Atmospheric Sounding (MIPAS), J. Geophys. Res., 109, D18301, https://doi.org/10.1029/2004JD004856, 2004.

Myhre, G., Shindell, D., Bréon, F., Collins, W., Fuglestvedt, J., Huang, J., Koch, D., Lamarque, J.-F., Lee, D., Mendoza, B., Nakajima, T., Robock, A., Stephens, G., Takemura, T., and Zhang, H.: Anthropogenic and Natural Radiative Forcing, in: Climate Change 2013: The Physical Science Basis. Contribution of Working Group I to the Fifth Assessment Report of the Intergovernmental Panel on Climate Change, edited by Stocker, T. F., Qin, D., Plattner, G.-K., Tignor, M., Allen, S. K., Boschung, J., Nauels, A., Xia, Y., Bex, V., and Midgley, P. M., Chapter 8, pp. 659—-740, Cambridge University Press, Cambridge, United Kingdom and New York, NY, USA, https://doi.org/10.1017/CBO9781107415324.018, 2014.

Noël, S., Bramstedt, K., Hilker, M., Liebing, P., Plieninger, J., Reuter, M., Rozanov, A., andH. Bovensmann, C. E. S., and Burrows, J. P.: Stratospheric CH_4 and CO_2 profiles derived from SCIAMACHY solar occultation measurements, Atmospheric Measurement Techniques, 9, 1485–1503, https://doi.org/10.5194/amt-9-1485-2016, 2016.

Oelhaf, H.: MIPAS Mission Plan, Tech. Rep. ENVI-SPPA-EOPG-TN-07-0073, ESA, 2008.

Park, J. H., Russell III, J. M., Gordley, L. L., Drayson, S. R., Benner, D. C., McInerney, J. M., Gunson, M. R., Toon, G. C., Sen, B., Blavier, J.-F., Webster, C. R., Zipf, E. C., Erdman, P., Schmidt, U., and Schiller, C.: Validation of Halogen Occultation Experiment CH_4 measurements from the UARS, J. Geophys. Res., 101, 10,183–10,203, https://doi.org/10.1029/95JD02736, 1996.

Phillips, D.: A Technique for the numerical solution of certain integral equations of first kind, J. Ass. Comput. Mat., 9, 84–97, https://doi.org/10.1145/321105.321114, 1962.

Plieninger, J., von Clarmann, T., Stiller, G. P., Grabowski, U., Glatthor, N., Kellmann, S., Linden, A., Haenel, F., Kiefer, M., Höpfner, M., Laeng, A., and Lossow, S.: Methane and nitrous oxide retrievals from MIPAS-ENVISAT, Atmos. Meas. Tech., 8, 4657–4670, https://doi.org/10.5194/amt-8-4657-2015, 2015.

Plieninger, J., Laeng, A., Lossow, S., von Clarmann, T., Stiller, G. P., Kellmann, S., Linden, A., Kiefer, M., Walker, K. A., Noël, S., Hervig, M., McHugh, M., Lambert, A., Urban, J., Elkins, J. W., and Murtagh, D.: Validation of revised methane and nitrous oxide profiles from MIPAS-ENVISAT, Atmos. Meas. Tech., 9, 765–779, https://doi.org/10.5194/amt-9-765-2016, 2016.

Plumb, R. A.: A "tropical pipe" model of stratospheric transport, J. Geophys. Res. Atmos., 101, 3957–3972, https://doi.org/10.1029/95jd03002, 1996.

Raspollini, P., Arnone, E., Barbara, F., Bianchini, M., Carli, B., Ceccherini, S., Chipperfield, M. P., Dehn, A., Della Fera, S., Dinelli, B. M., Dudhia, A., Flaud, J.-M., Gai, M., Kiefer, M., López-Puertas, M., Moore, D. P., Piro, A., Remedios, J. J., Ridolfi, M., Sembhi, H., Sgheri, L., and Zoppetti, N.: Level 2 processor and auxiliary data for ESA Version 8 final full mission analysis of MIPAS measurements on ENVISAT, Atmos. Meas. Tech., 15, 1871–1901, https://doi.org/10.5194/amt-15-1871-2022, 2022.

Ravishankara, A. R., Daniel, J. S., and Portmann, R. W.: Nitrous Oxide (N_2O): The Dominant Ozone–Depleting Substance Emitted in the 21st Century, Science, 326, 123–125, https://doi.org/10.1126/science.1176985, 2009.

Rodgers, C. D.: Inverse Methods for Atmospheric Sounding: Theory and Practice, vol. 2 of *Series on Atmospheric, Oceanic and Planetary Physics, F. W. Taylor, ed.*, World Scientific, doi:10.1142/3171, Singapore, New Jersey, London, Hong Kong, https://doi.org/10.1142/3171, 2000.

Rong, P. P., Russell III, J. M., Marshall, B. T., Siskind, D. E., Hervig, M. E., Gordley, L. L., Bernath, P. F., and Walker, K. A.: Version 1.3 AIM SOFIE measured methane (CH_4): Validation and Seasonal Climatology, J. Geophys.Res., 121, 13 158–13 179, https://doi.org/10.1002/2016JD025415, 2016.

Rothman, L. S., Gordon, I. E., Barbe, A., Benner, D. C., Bernath, P. F., Birk, M., Boudon, V., Browng, L. R., Campargueh, A., Champion, J.-P., Chance, K., Coudert, L. H., Dana, V., Devi, V. M., Fally, S., Flaud, J.-M., Gamache, R. R., Goldman, A., , Jacquemart, D., Kleiner, I., Lacome, N., Lafferty, W. J., Mandin, J.-Y., Massie, S., Mikhailenko, S. N., Miller, C. E., Moazzen-Ahmadi, N., Naumenko, O. V., Nikitin, A. V., Orphal, J., Perevalov, V. I., Perrin, A., Predoi-Cross, A., Rinsland, C. P., Rotger, M., Šimečková, M., Smith, M. A. H., Sung, K., Tashkun, S. A., Tennyson, J., Toth, R. A., Vandaele, A. C., and Vander Auwera, J.: The HITRAN 2008 molecular spectroscopic database, J. Quant. Spectrosc. and Radiat. Transfer, 110, 533–572, https://doi.org/https://doi.org/10.1016/j.jqsrt.2009.02.013, https://www.sciencedirect.com/science/article/pii/S0022407309000727, hITRAN, 2009.

Sheese, P. E., Walker, K. A., Boone, C. D., Bernath, P. F., and Funke, B.: Nitrous oxide in the atmosphere: First measurements of a lower thermospheric source, Geophys. Res. Lett., 43, 2866–2872, https://doi.org/10.1002/2015GL067353, http://dx.doi.org/10.1002/2015GL067353, 2015GL067353, 2016.

Shindell, D. T.: Climate and ozone response to increased stratospheric water vapor, Geophys. Res. Lett., 28, 1551–1554, https://doi.org/https://doi.org/10.1029/1999GL011197, https://agupubs.onlinelibrary.wiley.com/doi/abs/10.1029/1999GL011197, 2001.

Steck, T. and von Clarmann, T.: Constrained profile retrieval applied to the obervation mode of the Michelson Interferometer for Passive Atmospheric Sounding, Appl. Opt., 40, 3559–3571, https://doi.org/10.1364/AO.40.003559, https://opg.optica.org/ao/abstract.cfm?URI=ao-40-21-3559, 2001.

Steck, T., Höpfner, M., von Clarmann, T., and Grabowski, U.: Tomographic retrieval of atmospheric parameters from infrared limb emission observations, Appl. Opt., 44, 3291–3301, https://doi.org/10.1364/AO.44.003291, https://opg.optica.org/ao/abstract.cfm?URI=ao-44-16-3291, 2005.

Stiller, G. P., ed.: The Karlsruhe Optimized and Precise Radiative Transfer Algorithm (KOPRA), Forschungszentrum Karlsruhe, Karlsruhe, https://doi.org/10.5445/IR/270048971, doi:10.5445/IR/270048971, 22.02.11; LK 01; Wissenschaftliche Berichte, FZKA-6487 (Dezember 2000), 2000.

Stiller, G. P., von Clarmann, T., Funke, B., García-Comas, M., Glatthor, N., Grabowski, U., Kellmann, S., Kiefer, M., Laeng, A., Linden, A., and López-Puertas, M.: Version 8 IMK/IAA MIPAS reactive nitrogen, paper in preparation, 2023.

Strong, K., Wolff, M. A., Kerzenmacher, T. E., Walker, K. A., Bernath, P. F., Blumenstock, T., Boone, C., Catoire, V., Coffey, M., Mazière, M. D., Demoulin, P., Duchatelet, P., Dupuy, E., Hannigan, J., Höpfner, M., Glatthor, N., Griffith, D. W. T., Jin, J. J., Jones, N., Jucks, K., Kuellmann, H., Kuttippurath, J., Lambert, A., Mahieu, E., McConnell, J. C., Mellqvist, J., Mikuteit, S., Murtagh, D. P., Notholt, J., Piccolo, C., Raspollini, P., Ridolfi, M., Robert, C., Schneider, M., Schrems, O., Semeniuk, K., Senten, C., Stiller, G. P., Strandberg, A., Taylor, J., Tétard, C., Toohey, M., Urban, J., Warneke, T., and Wood, S.: Validation of ACE-FTS N_2O measurements, Atmos. Chem. Phys., 8, 4759–4786, https://doi.org/10.5194/acp-8-4759-2008, 2008.

Tikhonov, A.: On the solution of incorrectly stated problems and method of regularization, Dokl. Akad. Nauk. SSSR, 151, 501–504, 1963.

Toon, G. C., Farmer, C. B., Shaper, P. W., Lowes, L. L., Norton, R. H., Schoeberl, M. R., Lait, L. R., and Newman, P. A.: Evidence for Subsidence in the 1989 Arctic Winter Stratosphere from Airborne Infrared Composition Measurements, J. Geophys. Res., 97, 7963–7970, https://doi.org/https://doi.org/10.1029/91JD03115, https://agupubs.onlinelibrary.wiley.com/doi/abs/10.1029/91JD03115, 1992.

Tran, H., Flaud, P.-M., Gabard, T., Hase, F., von Clarmann, T., Camy-Peyret, C., Payan, S., and Hartmann, J.-M.: Model, software and database for line–mixing effects in the ν_3 and ν_4 bands of CH_4 and tests using laboratory and planetary measurements–I: N_2 (and air) broadenings and the earth atmosphere, J. Quant. Spectrosc. Radiat. Transfer, 101, 284–305, https://doi.org/https://doi.org/10.1016/j.jqsrt.2005.11.020, https://www.sciencedirect.com/science/article/pii/S0022407305003596, 2006.

Twomey, S.: On the Numerical Solution of Fredholm Integral Equations of the First Kind by the Inversion of the Linear System Produced by Quadrature, Journal of the ACM, 10, 97–101, https://doi.org/10.1145/321150.321157, https://doi.org/10.1145/321150.321157, 1963.

Urban, J., Lautié, N., Flochmoën, E. L., Jiménez, C., Eriksson, P., de La Noë, J., Dupuy, E., Ekström, M., El Amraoui, L., Frisk, U., Murtagh, D., Olberg, M., and Ricaud, P.: Odin/SMR limb observations of stratospheric trace gases: Level 2 processing of ClO, N_2O, HNO_3, and O_3, J. Geophys. Res., 110, D14307, https://doi.org/10.1029/2004JD005741, 2005a.

Urban, J., Lautié, N., Flochmoën, E. L., Jiménez, C., Eriksson, P., de La Noë, J., Dupuy, E., El Amraoui, L., Frisk, U., Jégou, F., Murtagh, D., Olberg, M., Ricaud, P., Camy-Peyret, C., Dufour, G., Payan, S., Huret, N., Pirre, M., Robinson, A. D., Harris, N. R. P., Bremer, H., Kleinböhl, A., Küllmann, K., Künzi, K., Kuttippurath, J., Ejiri, M. K., Nakajima, H., Sasano, Y., Sugita, T., Yokota, T., Piccolo, C., Raspollini, P., and Ridolfi, M.: Odin submillimeter radiometer limb observations of stratospheric trace gases: Validation of N_2O, J. Geophys. Res., 110, D09301, https://doi.org/10.1029/2004JD005394, 2005b.

Versick, S., Stiller, G. P., von Clarmann, T., Reddmann, T., Glatthor, N., Grabowski, U., Höpfner, M., Kellmann, S., Kiefer, M., Linden, A., Ruhnke, R., and Fischer, H.: Global stratospheric hydrogen peroxide distribution from MIPAS-Envisat full resolution spectra compared to KASIMA model results, Atmos. Chem. Phys., 12, 4923–4933, https://doi.org/10.5194/acp-12-4923-2012, 2012.

Volk, C. M., Elkins, J. W., Fahey, D. W., Salawitch, R. J., Dutton, G. S., Gilligan, J. M., Proffitt, M. H., Loewenstein, M., Podolske, J. R., Minschwaner, K., Margitan, J. J., and Chan, K. R.: Quantifying Transport Between the Tropical and Mid-Latitude Lower Stratosphere, Science, 272, 1763–1768, https://doi.org/10.1126/science.272.5269.1763, https://www.science.org/doi/abs/10.1126/science.272.5269.1763, 1996.

von Clarmann, T.: Smoothing error pitfalls, Atmos. Meas. Tech., 7, 3023–3034, https://doi.org/10.5194/amtd-7-3023-2014, 2014.

von Clarmann, T., Glatthor, N., Grabowski, U., Höpfner, M., Kellmann, S., Kiefer, M., Linden, A., Mengistu Tsidu, G., Milz, M., Steck, T., Stiller, G. P., Wang, D. Y., Fischer, H., Funke, B., Gil-López, S., and López-Puertas, M.: Retrieval of temperature and tangent altitude pointing from limb emission spectra recorded from space by the Michelson Interferometer for Passive Atmospheric Sounding (MIPAS), J. Geophys. Res., 108, 4736, https://doi.org/10.1029/2003JD003602, 2003.

von Clarmann, T., De Clercq, C., Ridolfi, M., Höpfner, M., and Lambert, J.-C.: The horizontal resolution of MIPAS, Atmos. Meas. Techn., 2, 47–54, https://doi.org/10.5194/amt-2-47-2009, 2009a.

von Clarmann, T., Höpfner, M., Kellmann, S., Linden, A., Chauhan, S., Funke, B., Grabowski, U., Glatthor, N., Kiefer, M., Schieferdecker, T., Stiller, G. P., and Versick, S.: Retrieval of temperature, H_2O, O_3, HNO_3, CH_4, N_2O, $ClONO_2$ and ClO from MIPAS reduced resolution nominal mode limb emission measurements, Atmos. Meas. Tech., 2, 159–175, https://doi.org/10.5194/amt-2-159-2009, 2009b.

von Clarmann, T., Funke, B., Glatthor, N., Kellmann, S., Kiefer, M., Kirner, O., Sinnhuber, B.-M., and Stiller, G. P.: The MIPAS HOCl climatology, Atmos. Chem. Phys., 12, 1965–1977, https://doi.org/10.5194/acp-12-1965-2012, 2012.

von Clarmann, T., Funke, B., López-Puertas, M., Kellmann, S., Linden, A., Stiller, G. P., Jackman, C. H., and Harvey, V. L.: The solar proton events in 2012 as observed by MIPAS, Geophys. Res. Lett., 40, 1–5, https://doi.org/10.1002/grl.50119, 2013.

von Clarmann, T., Glatthor, N., and Plieninger, J.: Maximum likelihood representation of MIPAS profiles, Atmos. Meas. Tech., 8, 2749–2757, https://doi.org/10.5194/amt-8-2749-2015, 2015.

von Clarmann, T., Degenstein, D. A., Livesey, N. J., Bender, S., Braverman, A., Butz, A., Compernolle, S., Damadeo, R., Dueck, S., Eriksson, P., Funke, B., Johnson, M. C., Kasai, Y., Keppens, A., Kleinert, A., Kramarova, N. A., Laeng, A., Langerock, B., Payne, V. H., Rozanov, A., Sato, T. O., Schneider, M., Sheese, P., Sofieva, V., Stiller, G. P., von Savigny, C., and Zawada, D.: Overview: Estimating and Reporting Uncertainties in Remotely Sensed Atmospheric Composition and Temperature, Atmos. Meas. Tech., 13, 4393–4436, https://doi.org/10.5194/amt-13-4393-2020, 2020.

von Clarmann, T., Grabowski, U., Stiller, G. P., Monge-Sanz, B. M., Glatthor, N., and Kellmann, S.: The middle atmospheric meridional circulation for 2002-2012 derived from MIPAS observations, Atmos. Chem. Phys., 21, 8823–8843, https://doi.org/10.5194/acp-21-8823-2021, 2021.

von Clarmann, T., Glatthor, N., Grabowski, U., Funke, B., Kiefer, M., Kleinert, A., Stiller, G. P., Linden, A., and Kellmann, S.: TUNER–compliant error estimation for MIPAS: methodology, Atmos. Meas. Tech., 15, 6991–7018, https://doi.org/10.5194/amt-15-6991-2022, https://amt.copernicus.org/articles/15/6991/2022/, 2022.

Figure 1. Top row: CH$_4$ error budget for daytime northern midlatitude summer conditions for FR (left) and RR (right) data, shown as percentage of the respective mean CH$_4$ profile. All error estimates are 1-σ uncertainties. Error contributions are marked "total", "random" and "syst" for the total, total random and total systematic error, further "T+LOS" for the propagated error from the T+LOS retrieval, "noise" for the error due to spectral noise, "spectro" for the spectroscopic error, "gain" for residual gain calibration uncertainties (MIPAS bands A and B), "shift" for the spectral shift error, "ILS" for the instrument line shape error, "offset" for the error due to spectral offset, and "interf" for the error due to interfering gases. Information on the ingoing uncertainties can be found in the text and in Tables 3 and 4. Bottom row: Same as top row, but for N$_2$O.
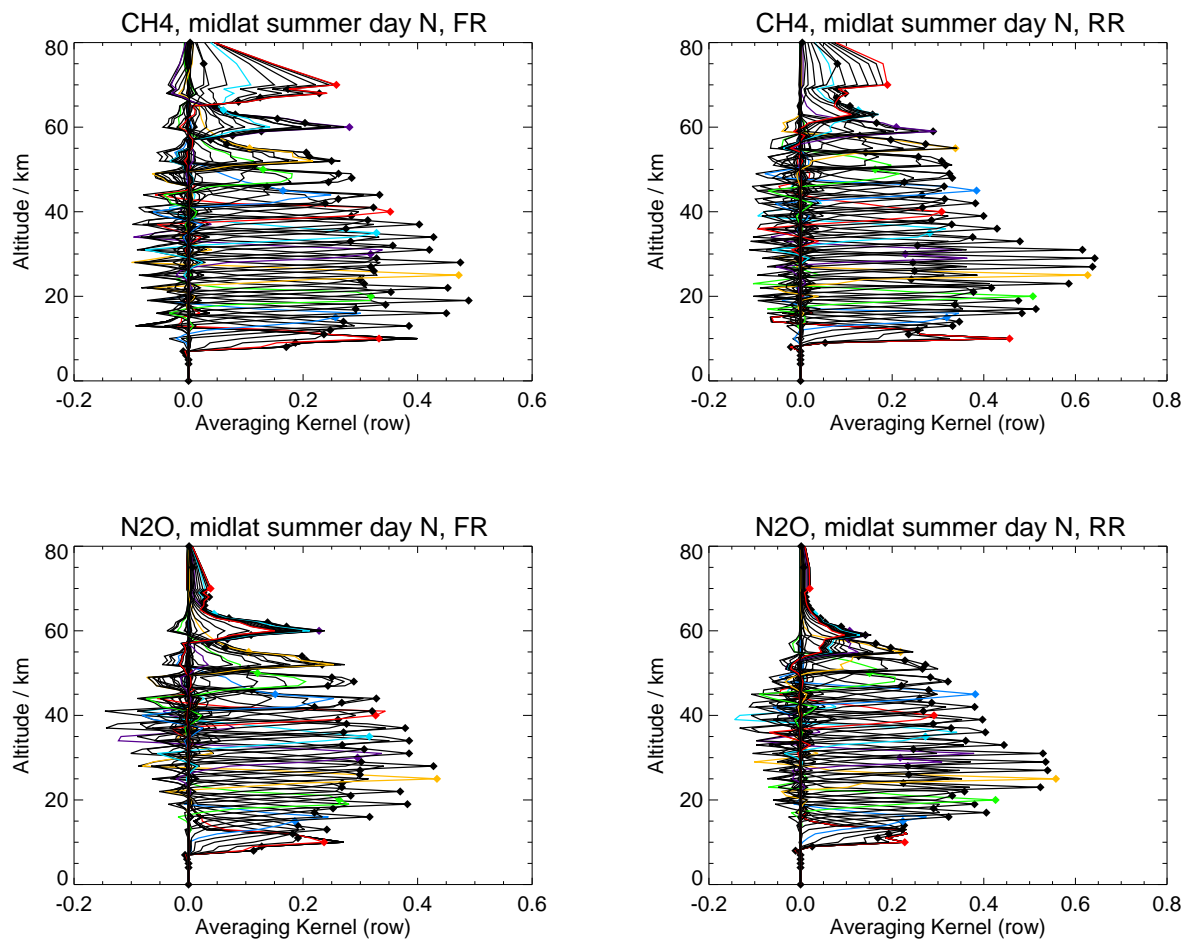
Figure 2. Top row: Rows of the averaging kernels belonging to a CH$_4$ profile measured at full spectral resolution (FR) at 55.70°N, 170.02°E on 10 October 2003 (left) and to a CH$_4$ profile measured at reduced spectral resolution (RR) at 41.02°N, 98.74°E on 26 December 2009 (right). Bottom row: Same as top row, but for N$_2$O. The diamonds indicate the nominal retrieval height. If the nominal retrieval height is located at the peak of the averaging kernel row, there is no vertical information displacement.
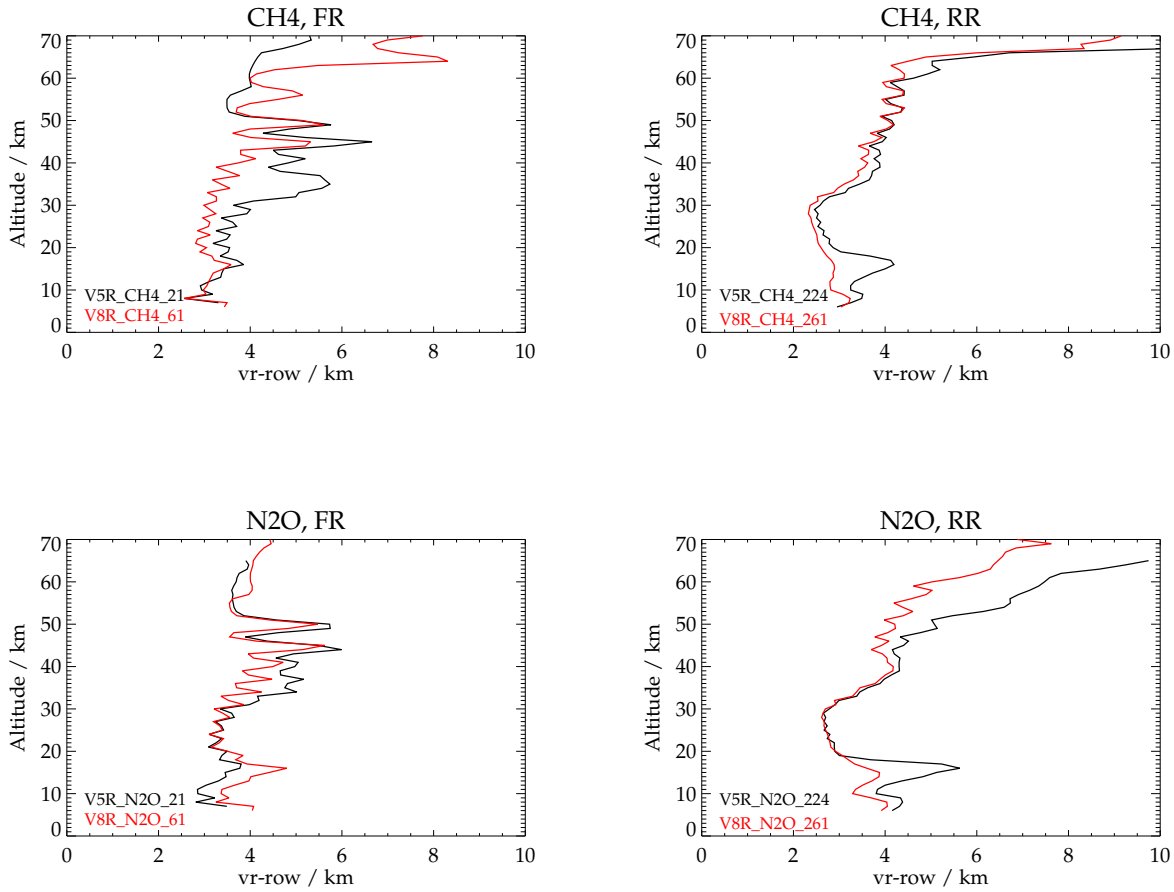
Figure 3. Top left: Vertical resolution of the CH_4 data product V5H_CH4_21 (black) and of the new data product V8H_CH4_61 (red), averaged over orbits 1753-1765 of the full spectral resolution period (FR). Top right: Vertical resolution of the CH_4 data products V5R_CH4_224 (black) and V8R_CH4_261, (red), averaged over orbits 29031-29051 of the reduced spectral resolution period (RR). Bottom row: Same as top row, but for N_2O.
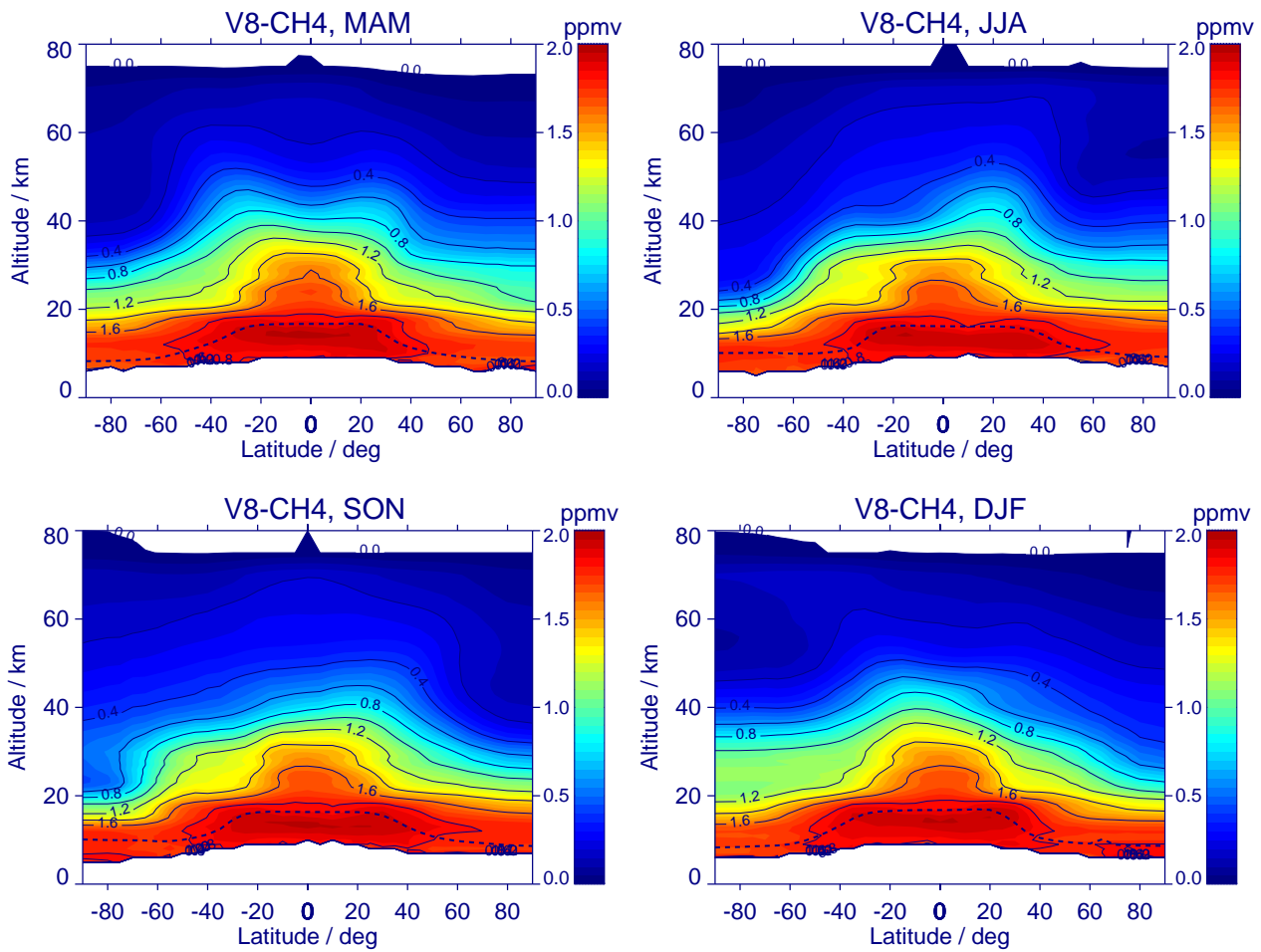
Figure 4. Zonal mean seasonal composites of V8-CH₄ retrieved from NOM FR and NOM RR measurements (2002-2012) during March to May (top left), June to August (top right), September to November (bottom left) and December to February (bottom right). The dotted line indicates the seasonal mean thermal tropopause.
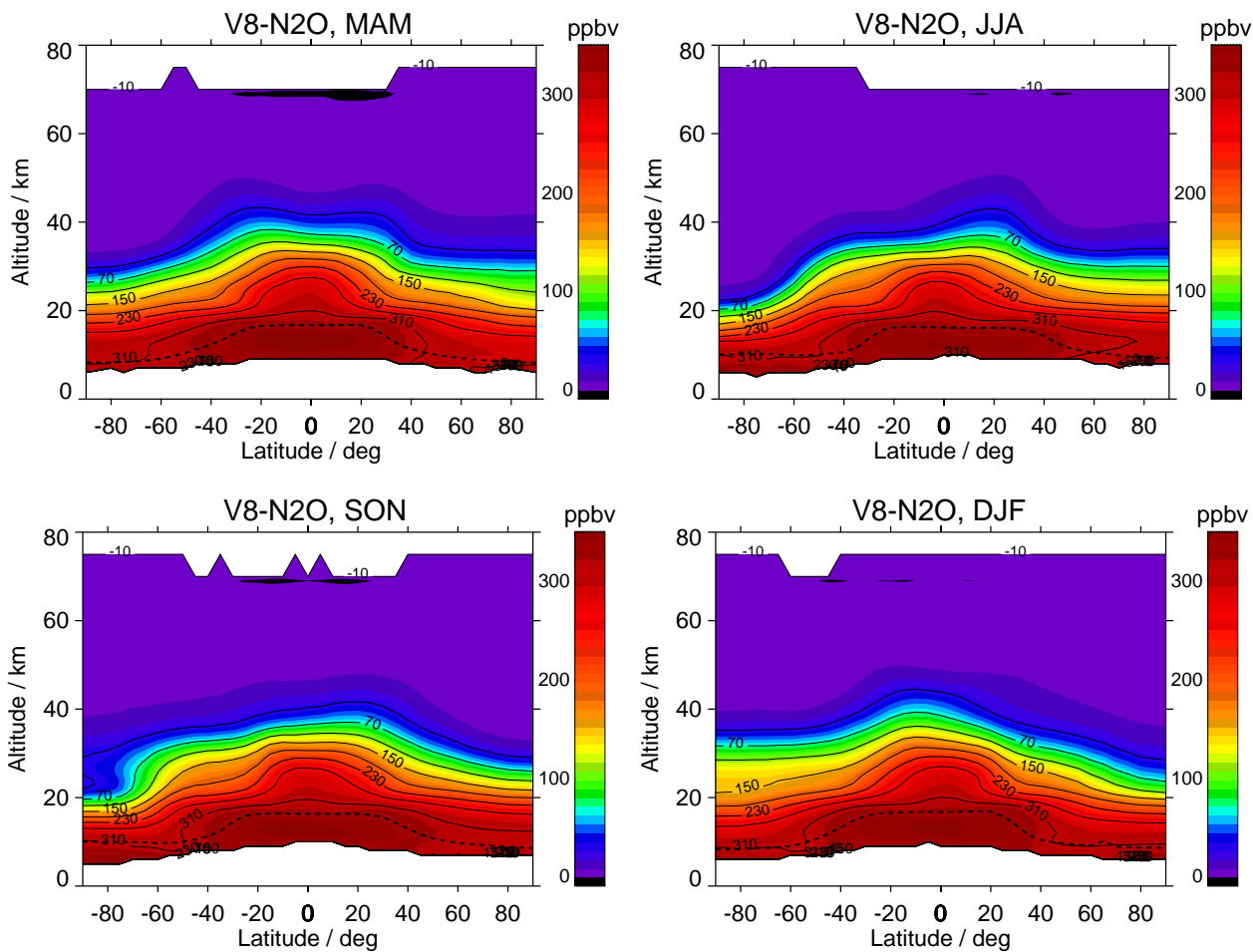
Figure 5. Zonal mean seasonal composites of V8-N$_2$O retrieved from NOM FR and NOM RR measurements (2002-2012) during March to May (top left), June to August (top right), September to November (bottom left) and December to February (bottom right). The dotted line indicates the seasonal mean thermal tropopause.
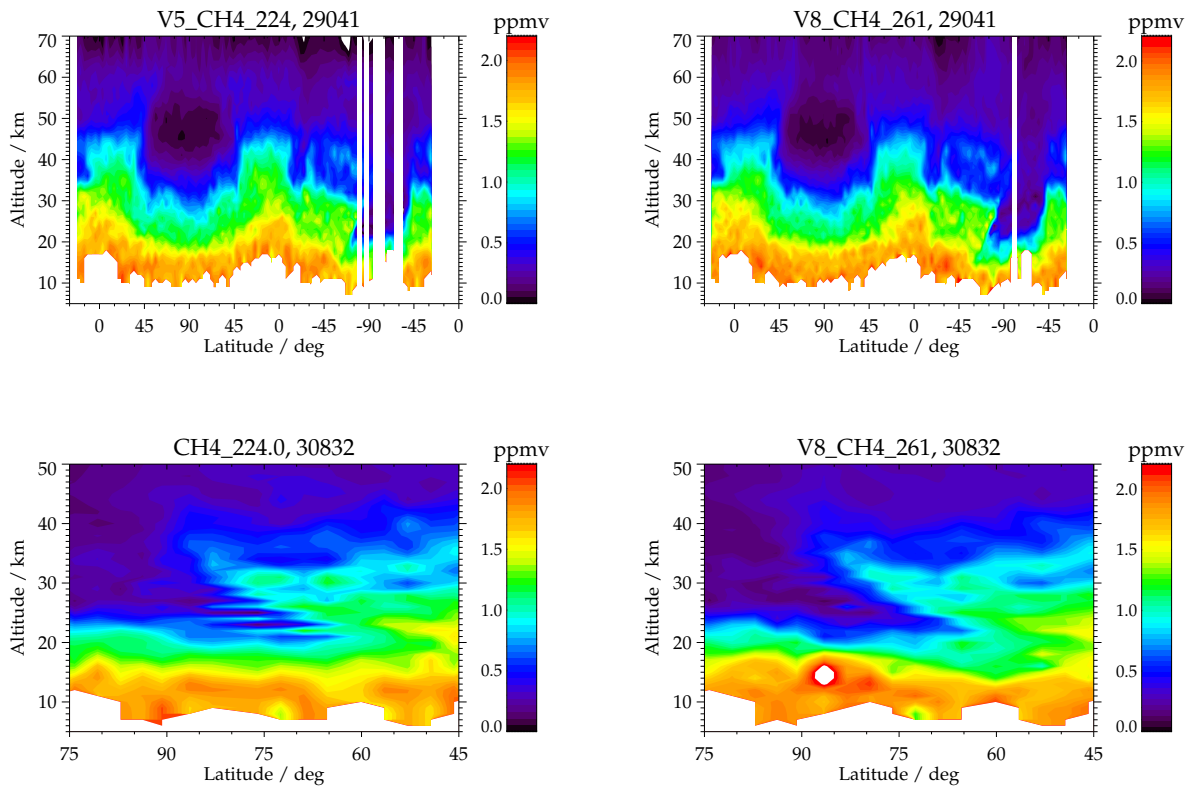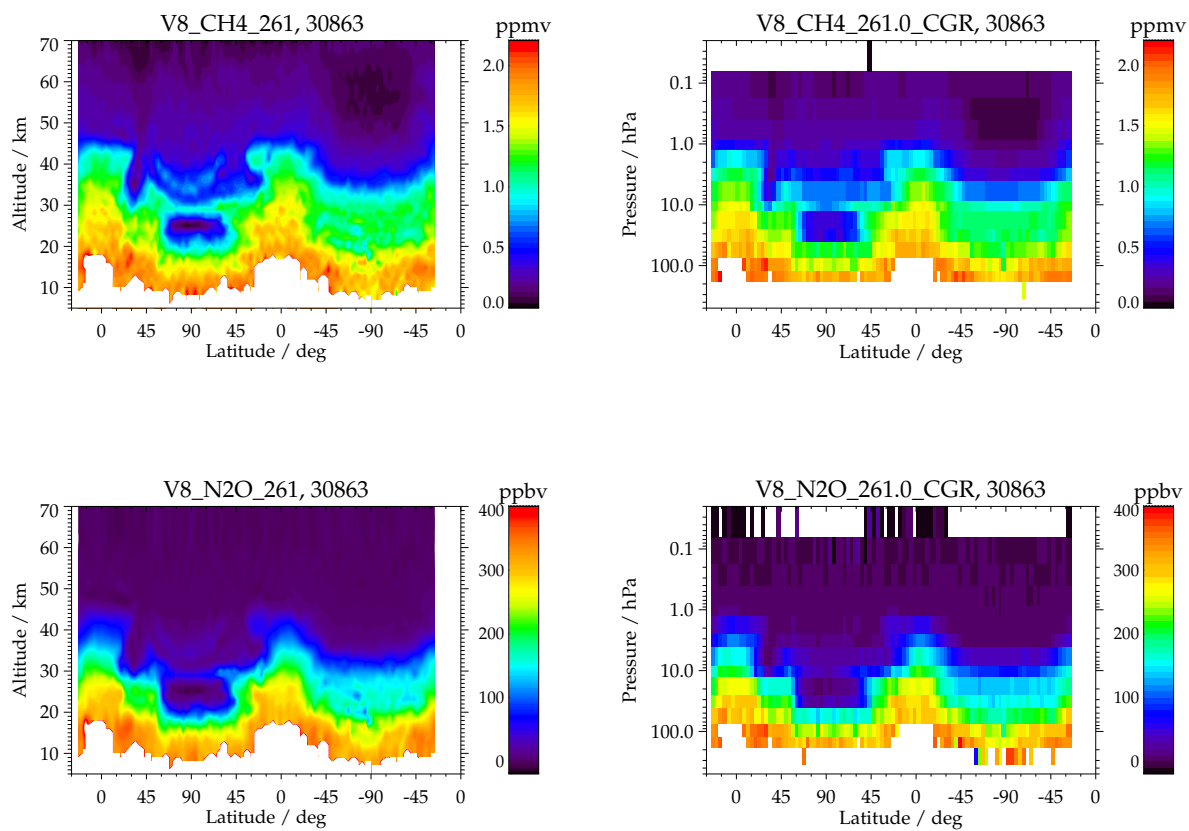
Figure 6. Top left: Latitude-height cross section of CH_4 version V5R_CH4_224, measured on 19 September, 2007, along orbit 29041. The white areas around 90°S represent scans with not converged retrievals. Top right: Same as left, but for version V8R_CH4_261, where the number of not converged scans has reduced to one. Bottom left: Latitude-height cross section of CH_4 version V5R_CH4_224, measured on 23 January, 2008, along the northern part of orbit 30832. Around 75°N at the descending part of the orbit (90°N -> 45°N) there are strongly oscillating profiles. Bottom right: Same as left, but for version V8R_CH4_261. The profiles around 75°N are considerably smoother.
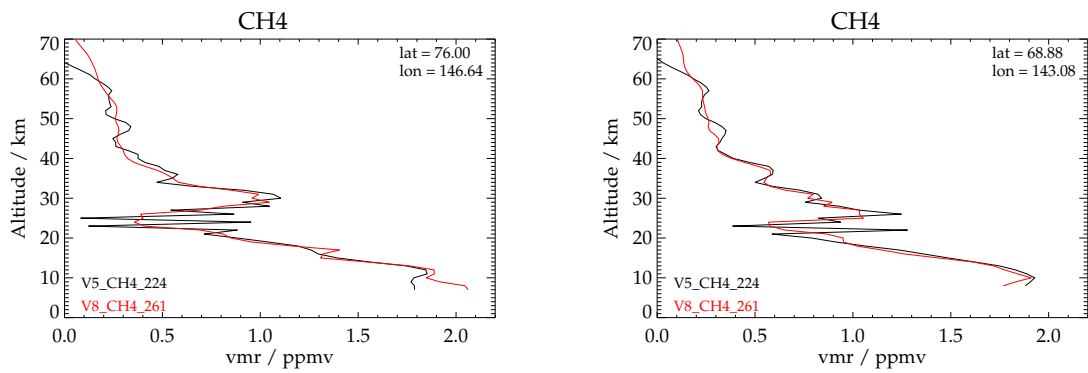
Figure 7. CH$_4$ profiles of orbit 30832, obtained at 76.00°N (left) and at 68.88°N (right) with retrieval setups V5R_CH4_224 (black) and V8R_CH4_261 (red). The new retrieval setup including horizontal CH$_4$- and N$_2$O-gradients as well as an oscillation detection in the iteration scheme leads to considerably reduced oscillations.
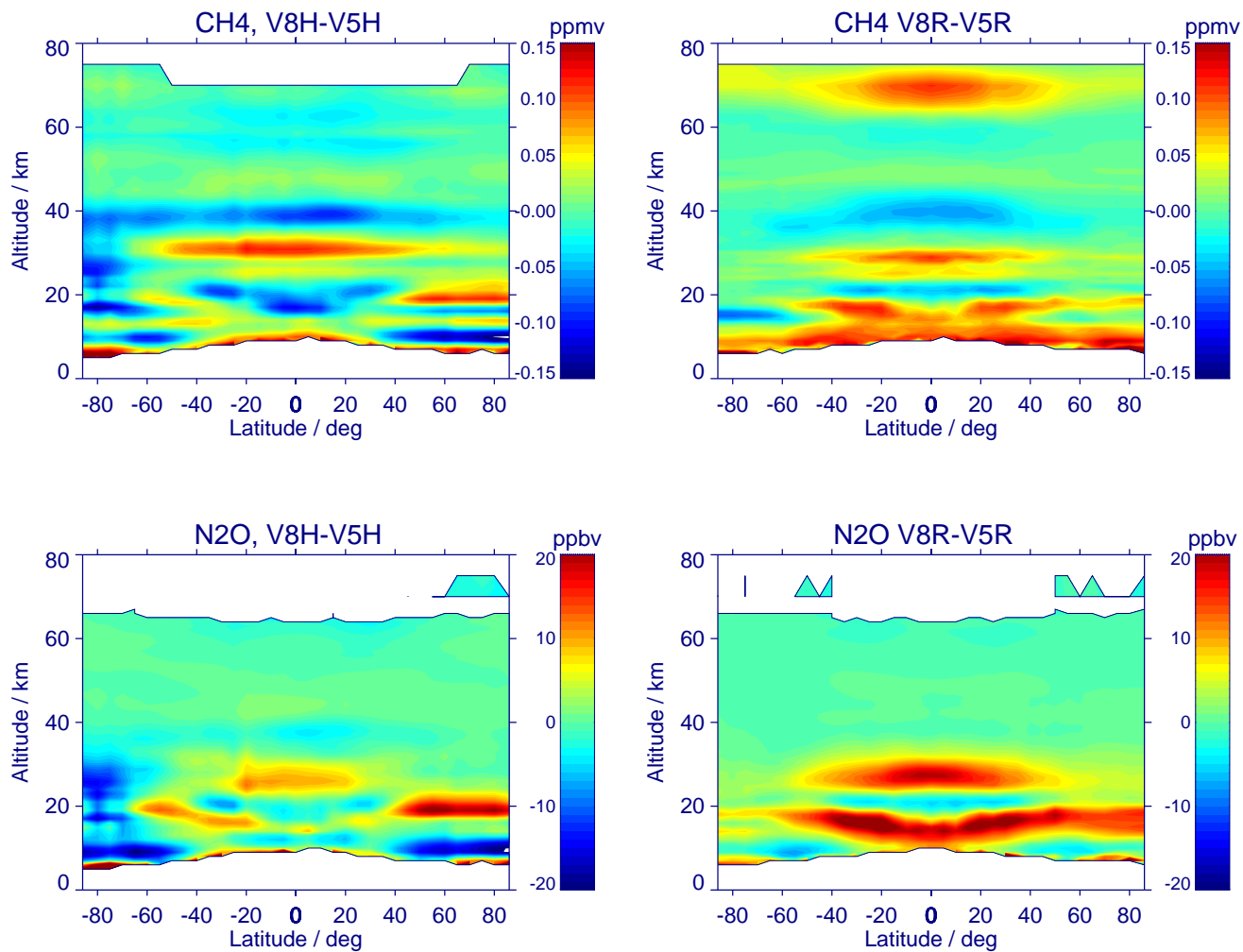
Figure 8. Top left: Zonal mean differences between MIPAS V8 and V5 CH_4-measurements at full (FR) spectral resolution (V8H_CH4_61, V5H_CH4_21) averaged over the period July 2002 to March 2004. Top right: Zonal mean differences between MIPAS V8 and V5 CH_4-measurements at reduced (RR) spectral resolution (V8R_CH4_161, V5R_CH4_261, V5R_CH4_120, V5R_CH4_224/225) averaged over the period January 2005 to April 2012. Bottom row: Same as top row, but for N_2O.

Figure 9. Top left: Latitude-height cross section of standard CH$_4$ retrieval (V8R_CH4_261) from measurements on 25 January, 2008, along orbit 30863. Top right: Corresponding coarse grid retrieval. Bottom row: Same as top row, but for N$_2$O.